PLK1 regulates CtIP and DNA2 interplay in long-range DNA end resection

Ilaria Ceppi,[1,2] Elda Cannavo,[1] Hélène Bret,[3] Rosa Camarillo,[4,5] Francesca Vivalda,[6] Roshan Singh Thakur,[1] Amador Romero-Franco,[4,5] Alessandro A. Sartori,[6] Pablo Huertas,[4,5] Raphaël Guérois,[3] and Petr Cejka[1,2]

[1]Institute for Research in Biomedicine, Faculty of Biomedical Sciences, Università della Svizzera italiana (USI), Bellinzona 6500, Switzerland; [2]Department of Biology, Institute of Biochemistry, Eidgenössische Technische Hochschule (ETH), Zürich 8093, Switzerland; [3]Institute for Integrative Biology of the Cell (I2BC), Commissariat à l'Energie Atomique, Centre National de la Recherche Scientifique, Université Paris-Sud, Université Paris-Saclay, Gif-sur-Yvette 91190, France; [4]Departamento de Genética, Facultad de Biología, Universidad de Sevilla, Sevilla 41080, Spain; [5]Centro Andaluz de Biología Molecular y Medicina Regenerativa (CABIMER), Universidad de Sevilla-Consejo Superior de Investigaciones Científicas-Universidad Pablo de Olavide, Sevilla 41092, Spain; [6]Institute of Molecular Cancer Research, University of Zürich, Zürich 8057, Switzerland

DNA double-strand break (DSB) repair is initiated by DNA end resection. CtIP acts in short-range resection to stimulate MRE11–RAD50–NBS1 (MRN) to endonucleolytically cleave 5′-terminated DNA to bypass protein blocks. CtIP also promotes the DNA2 helicase–nuclease to accelerate long-range resection downstream from MRN. Here, using AlphaFold2, we identified CtIP-F728E-Y736E as a separation-of-function mutant that is still proficient in conjunction with MRN but is not able to stimulate ssDNA degradation by DNA2. Accordingly, CtIP-F728E-Y736E impairs physical interaction with DNA2. Cellular assays revealed that CtIP-F728E-Y736E cells exhibit reduced DSB-dependent chromatin-bound RPA, impaired long-range resection, and increased sensitivity to DSB-inducing drugs. Previously, CtIP was shown to be targeted by PLK1 to inhibit long-range resection, yet the underlying mechanism was unclear. We show that the DNA2-interacting region in CtIP includes the PLK1 target site at S723. The integrity of S723 in CtIP is necessary for the stimulation of DNA2, and phosphorylation of CtIP by PLK1 in vitro is consequently inhibitory, explaining why PLK1 restricts long-range resection. Our data support a model in which CDK-dependent phosphorylation of CtIP activates resection by MRN in S phase, and PLK1-mediated phosphorylation of CtIP disrupts CtIP stimulation of DNA2 to attenuate long-range resection later at G2/M.

[*Keywords*: DNA end resection; DNA repair; homologous recombination; phosphorylation]

Supplemental material is available for this article.

Received August 4, 2022; revised version accepted January 12, 2023.

The repair of DNA double-strand breaks (DSBs) in eukaryotes is catalyzed by either of two main processes: end joining and homology-directed repair (Ranjha et al. 2018). The end-joining pathways, comprising both the canonical nonhomologous end joining (NHEJ) as well as the microhomology-mediated end joining (MMEJ), involve only minimal processing of the DNA ends, followed by the ligation of DNA molecules with little or no homology (Chang et al. 2017). In contrast, homology-directed repair pathways use an intact homologous DNA sequence, usually the sister chromatid in vegetative cells, as the repair template. Consequently, recombination is typically limited to the S and G2 phases of the cell cycle, when the sister chromatid is available (Ira et al. 2004; Bocquet et al. 2014; West et al. 2015; Ranjha et al. 2018). The DSB repair pathway is determined by DNA end resection. Although limited resection may be involved in NHEJ/MMEJ, extended resection inhibits end joining and commits DSB repair to the recombination pathways (Shibata et al. 2014; Cejka and Symington 2021).

DNA end resection involves a controlled degradation of the 5′-terminated DNA strand at DSB sites. It leads to 3′ overhangs, which are essential for the subsequent steps in homologous recombination. In most cases, resection is a two-step process divided into short-range and long-range pathways (Zhu et al. 2008; Cejka and Symington 2021). The first short-range step is catalyzed by the MRE11–RAD50–NBS1 (MRN) complex. CtIP, upon its phosphorylation by CDK, promotes the endonuclease activity of MRN. CtIP is thus an essential cofactor of MRN in short-range resection (Huertas et al. 2008; Huertas and Jackson 2009; Anand et al. 2016; Deshpande et al. 2016; Cannavo et al. 2018). The key CDK phosphorylation site

Corresponding author: petr.cejka@irb.usi.ch
Article published online ahead of print. Article and publication date are online at http://www.genesdev.org/cgi/doi/10.1101/gad.349981.122.

in CtIP is T847 near its C terminus, which is well conserved in evolution (Huertas et al. 2008; Huertas and Jackson 2009). However, CDK phosphorylates CtIP at additional sites localized in the central domain of CtIP, which allows it to interact with NBS1 and further promotes resection (Wang et al. 2013; Anand et al. 2019). The CDK-dependent step thus activates resection and hence homologous recombination only in the S/G2 phase of the cell cycle, when sister chromatids are available. Downstream from MRN, either of two resection pathways produce 3′ ssDNA overhangs up to several kilobases in length. These long-range pathways are catalyzed by EXO1 or DNA2 nucleases (Gravel et al. 2008; Mimitou and Symington 2008; Zhu et al. 2008; Cejka and Kowalczykowski 2010). EXO1 resects the 5′-terminated DNA strand within dsDNA (Tran et al. 2002; Cannavo et al. 2013). DNA2 instead degrades 5′-terminated ssDNA and thus requires a helicase partner, which can be either BLM or WRN in human cells. The cognate helicase unwinds dsDNA to provide ssDNA for the nucleolytic degradation by DNA2 (Bae et al. 1998; Masuda-Sasa et al. 2006; Cejka et al. 2010; Nimonkar et al. 2011; Sturzenegger et al. 2014; Pinto et al. 2016). DNA2 also possesses a helicase domain, which likely functions as a ssDNA translocase to facilitate movement along the unwound ssDNA. The enhanced DNA2 translocation ultimately promotes DNA degradation by the DNA2 nuclease domain, in particular in the presence of the replication protein A (RPA) (Zhou et al. 2015; Pinto et al. 2016; Levikova et al. 2017; Miller et al. 2017; Ceppi et al. 2020; Acharya et al. 2021; Shen et al. 2022).

Despite DNA end resection being commonly described as a two-step process, the short- and long-range resection pathways and their respective nucleases are not independent. The MRN complex has a structural role in promoting DNA2- and EXO1-dependent resection (Cejka et al. 2010; Shim et al. 2010; Nimonkar et al. 2011; Cannavo et al. 2013; Shibata et al. 2014; Reginato et al. 2017; Gobbini et al. 2018). In addition to its role in promoting the endonuclease activity of MRN, CtIP was found to stimulate DNA2-mediated long-range resection in vitro by enhancing DNA unwinding by BLM as well as the motor activity of DNA2 in vitro (Daley et al. 2017; Ceppi et al. 2020). Simultaneously, CtIP interacts with EXO1 and restrains its processive 5′–3′ exonuclease activity in vitro, implicating CtIP in the modulation of long-range resection pathways (Eid et al. 2010). While the stimulation of short-range resection by CtIP and its regulation are relatively well understood, the function of CtIP in long-range resection is less clear. As the CtIP function upstream in short-range resection is prerequisite for resection and recombination, the downstream function in long-range resection is more difficult to address in cellular experiments.

Here, using molecular modeling by AlphaFold2 (Jumper et al. 2021), we precisely define the interaction between DNA2 and CtIP. We identified two conserved residues, F728 and Y736, in CtIP that are necessary for the physical and functional interaction with DNA2. The CtIP-F728E-Y736E mutant fails to bind DNA2 and cannot stimulate DNA2 activity to degrade ssDNA but is fully proficient in activating the MRN endonuclease. The CtIP-F728E-Y736E is thus a separation-of-function variant that allows definition of the physiological relevance of CtIP and DNA2 interplay in long-range resection pathway in human cells. Using multiple complementary cellular approaches, we found that CtIP-F728E-Y736E impairs long-range resection in vivo, which inhibits recombination and results in sensitivity to DNA-damaging drugs. PLK1 was previously shown to act on CtIP to inhibit long-range resection, but the underlying mechanism remained unclear (Wang et al. 2018). We note that the PLK1 target S723 lies within the DNA2 interaction patch in CtIP and show that the integrity of S723 in CtIP is important for physical interaction and, correspondingly, for the ability of CtIP to promote DNA2. In vitro phosphorylation of CtIP by PLK1 similarly inhibited CtIP function in long-range resection. Our results support a model in which CDK-dependent phosphorylation of CtIP early in the cell cycle in S phase activates MRN function in short-range resection, while PLK1-dependent phosphorylation of CtIP late in the cell cycle at G2/M then disrupts the stimulatory effect of CtIP on DNA2 to down-regulate long-range resection.

Results

Identification of CtIP separation-of-function point mutants deficient in promoting DNA2

The CtIP region between residues 690 and 740 was previously identified to be required for the stimulation of DNA2 motor activity (Ceppi et al. 2020), but a precise mapping of this physical and functional interplay was missing. To better define the interaction interface, we first performed multiple sequence alignment analysis of the respective CtIP regions in CtIP orthologs to reveal evolutionary patterns that could best fit with the ability to bind and activate the DNA2 helicase. A priori, we considered that no equivalent region should be present in unicellular organisms such as yeast, since the regulation of DNA2 by CtIP appeared to be restricted to higher eukaryotes (Ceppi et al. 2020). We identified that in the domain spanning positions 710–740, several residues were highly conserved among vertebrates, especially S723, F728, and Y736, while in mollusks and in more distantly related species, this conservation pattern was lost (Fig. 1A). It was previously shown that in nocodazole-arrested cells, S723, together with T693 and T731, can be phosphorylated by PLK1 upon its binding to CtIP, which is facilitated by CDK1/Aurora A-mediated phosphorylation on CtIP S327 (Wang et al. 2018). The conservation pattern of F728 and Y736 in the vicinity of S723 and the propensity of aromatic residues in disordered regions to mediate protein interactions prompted us to mutate F728 and Y736 to potentially affect CtIP binding to DNA2.

The prediction that F728 and Y736 may be involved in the interaction with DNA2 was further supported by the structural modeling of the assembly between DNA2 and CtIP region 690–740, which could be performed using

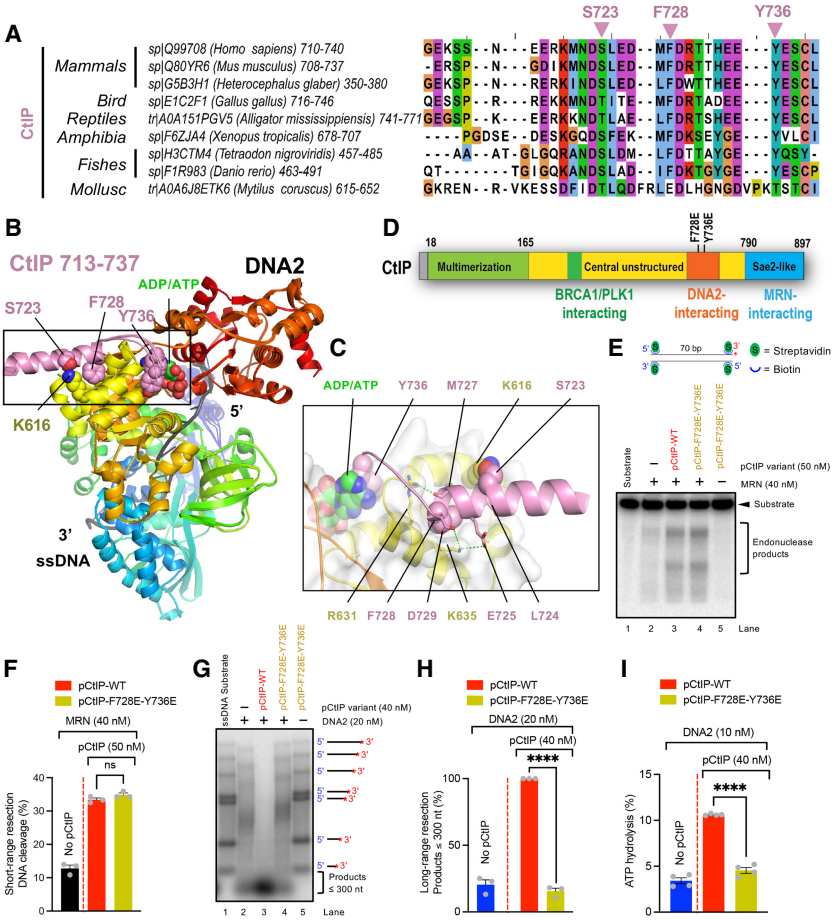

Figure 1. The CtIP-F728E-Y736E mutant separates CtIP functions in short- and long-range resection in vitro. (*A*) Multiple sequence alignment of orthologs of *Homo sapiens* CtIP focused on the domain spanning positions 710–740. (*B*) Superimposition of the structural models of the assembly between *H. sapiens* DNA2 (rainbow cartoon) and domain 720–737 of *H. sapiens* CtIP (pink cartoon), generated using AlphaFold2 from a coalignment of sequences. CtIP F728, highlighted as a sphere, is predicted to play an anchoring role in the interface and was mutated in the study. CtIP S723 is shown as sphere together with the conserved DNA2 K616, which is predicted to interact with the S723 side chain. The ADP/ATP molecule involved in the helicase activity of DNA2 is shown as green spheres, as observed in the structure of the mouse DNA2 (PDB: 5EAX). It occupies the same site as the predicted position of CtIP Y736, shown as a sphere. The location of CtIP Y736 varies significantly among the five models, in contrast to F728, whose position is very well defined, suggesting that Y736 may form more specific interactions with the nucleotide, which is not modeled by AlphaFold2. The position of ssDNA in DNA2, as observed in the structure of the mouse DNA2 (PDB: 5EAX), is indicated as gray sticks. (*C*) A magnified view of the interface highlighting the three CtIP residues: L724 and M727, which are predicted to bury with F728 in the hydrophobic cavity at the surface of DNA2. Conserved acidic positions E725 and D729 in the CtIP helix are predicted to form a salt bridge with DNA2 K635 (shown in yellow). (*D*) A schematic representation of the CtIP protein with the indicated F728 and Y736 residues mutated in the study. (*E*) A representative 15% denaturing polyacrylamide gel showing an endonuclease assay using 40 nM recombinant MRN complex and 50 nM indicated pCtIP variant on 3′ end-labeled 70-bp dsDNA with all ends blocked with streptavidin. The red asterisk indicates the position of the radioactive label. (*F*) Quantitation of overall DNA cleavage from experiments such as shown in *E*. $n = 3$; error bars indicate SEM. (ns) $P > 0.05$ (not significant), two-tailed *t*-test. (*G*) Degradation of ssDNA fragments of various length by 20 nM DNA2 without or with 40 nM indicated pCtIP variant in the presence of 864 nM RPA. Red asterisks indicate the position of the radioactive labels. (*H*) Quantitation of small degradation products (≤300 nt) from experiments such as shown in *G*. $n = 3$; error bars indicate SEM. (****) $P < 0.0001$, two-tailed *t*-test. (*I*) Quantitation of ATP hydrolysis from experiments such as shown in Supplemental Figure S1I. $n = 4$; error bars indicate SEM. (****) $P < 0.0001$, two-tailed *t*-test.

AlphaFold2 algorithm (Jumper et al. 2021). AlphaFold2 network parameters trained on the monomer or the multimer data sets converged toward a consistent solution, with the multimer-trained network resulting in a more robust and extensive interface observed in all five generated models (Fig. 1B). The predicted model with the highest pTMscore (0.84) exhibited low PAE (predicted alignment error) in the positions of CtIP, in contact to the interface (Supplemental Fig. S1A). High-confidence prediction was centered on CtIP F728, with residues 719–730 folding into a helix, which would anchor in an exposed apolar cavity at the surface of DNA2 formed by helices spanning residues 614–624 and 628–639 (Fig. 1C). The predicted interface would be stabilized by a network of favorable contacts (1) between the apolar residues of CtIP (L724, M727, and F728) and the DNA2 apolar cavity (Supplemental Fig. S1B), (2) between oppositely charged residues of CtIP (E725 and D729) with DNA2 K635 (Supplemental Fig. S1C), and (3) by a C-terminal capping by DNA2 R631 of the established CtIP helix (Fig. 1B). Remarkably, these residues in CtIP were also the most conserved residues in vertebrates (Fig. 1A). Moreover, the mapping of the evolutionary rates at the surface of either human or yeast DNA2 analyzed from multiple sequence alignments restricted either to vertebrates or fungal species highlighted that the DNA2 surface patch interacting with CtIP was specifically conserved in vertebrates but not in more remotely related species (Supplemental Fig. S1D,E). With regard to Y736, the five models did not converge toward a single conformation, suggesting a more speculative character of the prediction.

Based on the sequence alignment and structure prediction, we designed the CtIP-F728E-Y736E mutant as the most likely candidate to block the interaction with

DNA2 (Fig. 1D). At the same time, we anticipated that DNA2-L623E-K635E-L639E (referred to here as DNA2-EEE) would reciprocally disrupt the interaction with CtIP from the DNA2 side (Supplemental Fig. S1F). We then expressed and purified the wild-type and mutant CtIP and DNA2 variants in *Sf*9 insect cells (Supplemental Fig. S1G,H; Anand et al. 2016; Pinto et al. 2016; Ceppi et al. 2020). CtIP was prepared with phosphatase inhibitors, as established previously, to preserve CtIP phosphorylation at multiple positions in the polypeptide (Anand et al. 2016, 2019). Phosphorylation of CtIP is crucial for the stimulation of MRE11 endonuclease activity (Anand et al. 2016, 2019). Phosphorylated CtIP is referred to here as pCtIP.

The purified pCtIP-F728E-Y736E mutant was then used in in vitro reconstituted nuclease reactions with MRN or DNA2 to validate the model. First, we used radioactively labeled oligonucleotide-based dsDNA with streptavidin bound to DNA ends to investigate pCtIP-stimulated endonucleolytic DNA cleavage by MRN near protein-blocked DNA ends (Anand et al. 2016). We observed that wild-type pCtIP and the F728E-Y736E mutant stimulated the endonuclease of MRN to a similar extent, and hence pCtIP-F728E-Y736E exhibits no apparent defect in short-range resection in vitro (Fig. 1E,F). We next used a procedure developed previously that allows assessment of the function of DNA2 in long-range resection (Levikova et al. 2017; Ceppi et al. 2020). Specifically, we monitored the 5′ → 3′ degradation of 3′ end-labeled fragments of long ssDNA by DNA2 in the presence of RPA, which bypasses the need to use BLM. As BLM is also regulated by CtIP, the assay that we used is best suited to define the effect of CtIP on DNA2 (Daley et al. 2017; Ceppi et al. 2020). Strikingly, the pCtIP-F728E-Y736E variant was completely deficient in the stimulation of ssDNA degradation by DNA2 (Fig. 1G,H). Consistently, the pCtIP-F728E-Y736E variant failed to promote the ATPase activity of DNA2, in contrast to wild-type CtIP, in assays containing RPA and ssDNA as cofactors (Fig. 1I; Supplemental Fig. S1I). Collectively, our data indicate that CtIP-F728E-Y736E is a separation-of-function mutant that is proficient in its function as a cofactor of MRN in short-range resection but deficient in the stimulation of DNA2 in vitro.

CtIP-F728E-Y736E fails to interact with DNA2 and promote its motor-driven activities

Previously, we observed that the motor activity of yeast Dna2 led to an increase in the length of DNA degradation products (Levikova et al. 2017). The length of the DNA fragments may be important for DNA damage checkpoint activation or innate immune signaling through cGAS-STING, which was found to be dependent on DNA2 in human cells upon replication stress (Emam et al. 2022). Considering the enhancement of the human DNA2 motor by CtIP, we set out to test whether the length of DNA degradation products might be affected in the human system. To this point, we used biochemical reconstitution assays with DNA2 in the presence or absence of pCtIP. As a substrate, we used a 2200-nt-long ssDNA labeled internally at random locations, which allowed us to monitor degradation fragment lengths as opposed to experiments with end-labeled substrate. Kinetic experiments showed that in the absence of pCtIP, wild-type DNA2, similar to the helicase-deficient DNA2-K654R variant, mostly generated products <20 nt long at any time point tested (Fig. 2A,B; Supplemental Fig. S2A). In contrast, the presence of pCtIP with wild-type DNA2 yielded first long fragments, which were further degraded into smaller products at later time points (Fig. 2A,B), reminiscent of the reactions with yeast recombinant proteins (Levikova et al. 2017). In contrast, only short ssDNA degradation products were observed by helicase-deficient DNA2-K654R, irrespective of the presence of pCtIP (Supplemental Fig. S2A), confirming the need for an intact DNA2 motor activity for the generation of longer fragments in the presence of CtIP. In accord with this, we observed that the pCtIP-F728E-Y736E mutant also failed to promote the formation of long ssDNA degradation intermediates with wild-type DNA2 (Fig. 2A,B). Therefore, the two aromatic residue mutations in CtIP disrupt its interplay with DNA2, which is dependent on the stimulation of DNA2 motor activity.

Using pull-down assays with the recombinant proteins, we next observed that the pCtIP-F728E-Y736E mutant was strongly impaired in its ability to physically interact with DNA2 (Fig. 2C–E). We also observed that the DNA2-EEE mutant reciprocally disrupted the interaction with pCtIP, supporting the structural model (Supplemental Figs. S1F, S2B,C). However, DNA2-EEE was, per se, deficient in ssDNA degradation (Supplemental Fig. S2D,E), suggesting that the L623E-K635E-L639E mutations may have a broader impact on DNA2 structure and function. Indeed, the DNA2 nuclease domain contains a conserved iron sulfur cluster domain that coordinates nuclease and helicase activities and is generally very sensitive to mutagenesis (Mariotti et al. 2020). Therefore, we did not use DNA2-L623E-K635E-L639E for further analysis. Coimmunoprecipitation experiments in HEK293T cells cotransfected with FLAG-DNA2 and GFP-CtIP confirmed that the F728E-Y736E mutations impaired the interaction with DNA2 (Fig. 2F,G), although we note that the interaction in cell extracts was very weak. In agreement with its ability to stimulate the MRN endonuclease activity (Fig. 1E,F), pCtIP-F728E-Y736E was proficient in its ability to physically interact with MRE11, as well as with BRCA1, in vitro (Fig. 2H,I). Therefore, based on our in vitro and cellular experiments, the F728E-Y736E mutations in CtIP disrupted physical and functional interactions with DNA2 while not affecting the interplay with MRN, demonstrating that it is a useful separation-of-function mutant for cellular experiments.

The CtIP-F728E-Y736E mutant inhibits DNA2-dependent long-range resection in cells

We next set out to define the biological significance of the DNA2 interplay with CtIP using the predicted and in vitro validated CtIP-F728E-Y736E separation-of-function mutant. The DNA2-dependent long-range resection is at

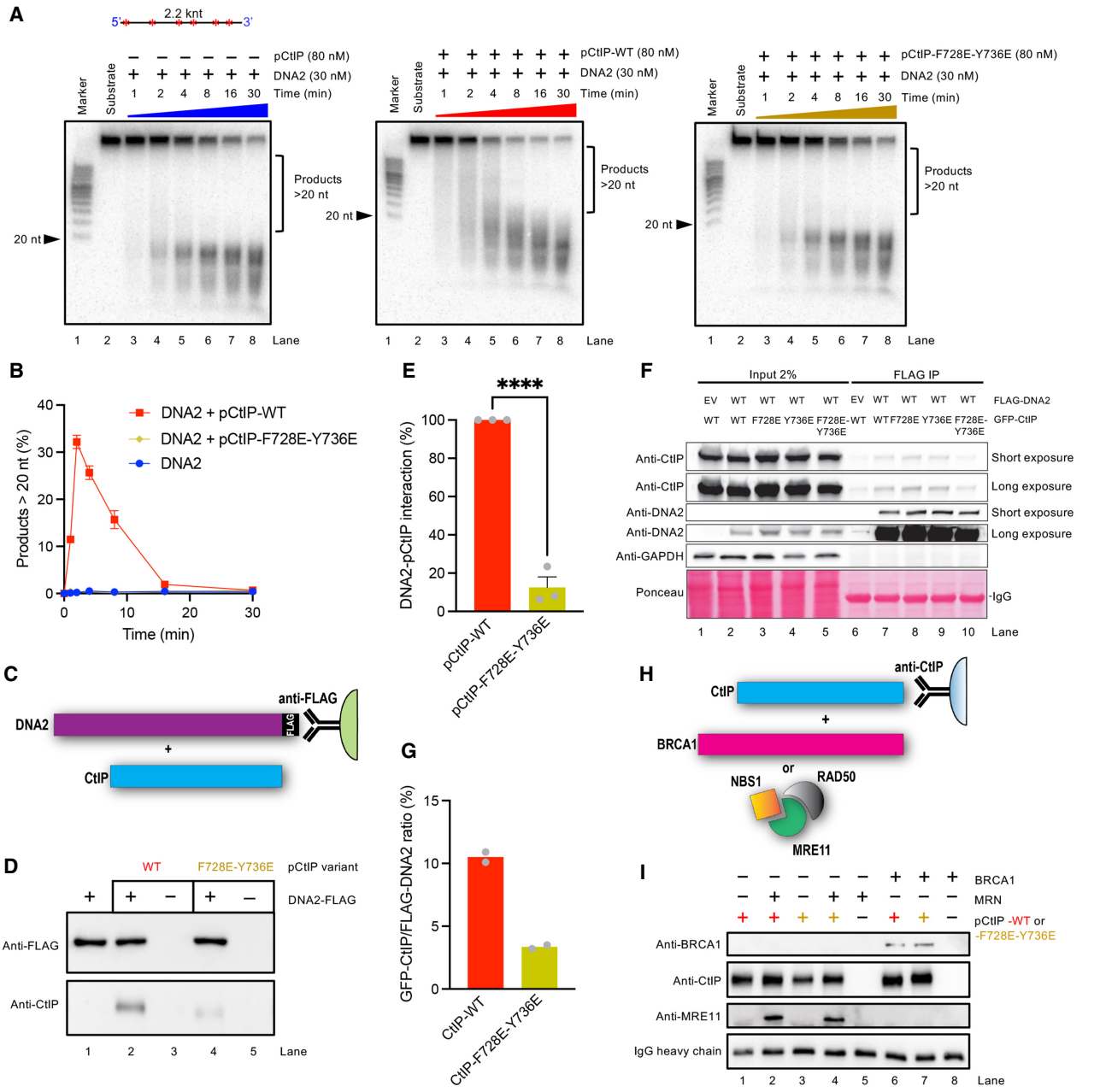

Figure 2. CtIP-F728E-Y736E fails to interact with DNA2 and promote its motor-driven activities. (*A*) Kinetics of randomly labeled 2200-nt-long ssDNA degradation by 30 nM wild-type DNA2 in the absence or presence of 80 nM either pCtIP wild type or pCtIP-F728E-Y736E mutant as analyzed by 20% polyacrylamide denaturing gels. Red asterisks indicate the position of the labels. Lane *1* shows radioactively labeled marker. The assay contained 395.5 nM RPA. (*B*) Quantitation of >20-nt products from experiments such as shown in *A*. $n = 3$; error bars indicate SEM. (*C*) Schematic of the pull-down assay with immobilized DNA2-FLAG and pCtIP variants. (*D*) Analysis of DNA2 interaction with wild-type pCtIP or pCtIP-F728E-Y736E. DNA2-FLAG was immobilized on M2 anti-FLAG affinity resin and incubated with the indicated recombinant pCtIP variant. The Western blot was performed with anti-FLAG and anti-CtIP antibodies. (*E*) Quantitation of the DNA2–pCtIP interaction from experiments such as shown in *D*. $n = 3$; error bars indicate SEM. (****) $P < 0.0001$, two-tailed *t*-test. (*F*) Coimmunoprecipitation experiments in extracts from HEK293T cells cotransfected with FLAG-DNA2 or empty vector (EV) and GFP-CtIP wild type (WT) or F728E and Y736E as single or double mutants. Cell lysates were incubated with M2 anti-FLAG beads overnight. The Western blot was performed with anti-CtIP, anti-DNA2, and anti-GAPDH antibodies. (*G*) Quantitation of the DNA2–CtIP interaction from experiments such as shown in *F*. Relative GFP-CtIP-WT and F728E-Y736E protein levels were determined by quantification of GFP-CtIP band intensity normalized to FLAG-DNA2 band intensity (bait) in the IP using ImageJ software. Averages shown, $n = 2$. (*H*) Schematic of the pull-down assay with immobilized CtIP (bait) and either MRE11 or BRCA1 (prey). (*I*) Analysis of wild-type pCtIP or pCtIP-F728E-Y736E interaction with MRE11 or BRCA1. The indicated recombinant pCtIP variant was immobilized on Dynabeads protein G (Invitrogen) conjugated with anti-CtIP antibody and incubated with MRE11 or BRCA1. The Western blot was performed with anti-CtIP, anti-MRE11, and anti-BRCA1 antibodies.

least partially redundant with the EXO1 pathway (Gravel et al. 2008; Mimitou and Symington 2008; Zhu et al. 2008; Nimonkar et al. 2011). To specifically analyze the effect of CtIP on long-range end resection by DNA2 in vivo, we first generated CRISPR/Cas9-based *EXO1* knockout clones in U2OS-SA and U2OS-EJ2 cells (Bennardo et al. 2008), DIvA (AsiSI-ER-U2OS) cells (Zhou et al. 2014), and HEK293 Flp-In T-REx cells (Supplemental Fig. S3A, B) and used them in the experiments described below. Additionally, we used the Flp-In system to produce *EXO1*$^{-/-}$ stable human HEK293 Flp-In T-REx cell lines with doxycycline-inducible expression of siRNA-resistant FLAG-tagged CtIP either wild type or F728E-Y736E mutant (Supplemental Fig. S3C). In these cells, the addition of 0.5 ng/mL doxycycline (DOX) for 48 h resulted in expression level of the two CtIP variants only moderately higher than that of endogenous CtIP (Supplemental Fig. S3D, cf. lanes 3,7 and 1).

We first evaluated the growth of stably CtIP-expressing *EXO1*$^{-/-}$ HEK293 Flp-In T-REx cells in the absence of DNA damage. Our data showed a clear decrease in the growth rate upon depletion of endogenous CtIP with siRNA, as expected (Fig. 3A; Supplemental Fig. S3E). We then observed an increase in cell counts upon doxycycline-induced expression of wild-type CtIP but not CtIP-F728E-Y736E (Fig. 3A), indicating that the F728E-Y736E mutations may affect CtIP functions even in the absence of exogenous DNA damage. Next, we investigated the accumulation of chromatin-bound replication protein A (RPA) after DSB induction with the DNA topoisomerase I inhibitor camptothecin (CPT). As RPA accumulates on ssDNA generated by resection, the assay offers first insights into the efficacy of resection (Forment et al. 2012). To this point, we used the *EXO1*$^{-/-}$ HEK293 Flp-In T-REx cells stably expressing wild-type or CtIP-F728E-Y736E variants in which endogenous CtIP was depleted with siRNA (Supplemental Fig. S3E). The RPA accumulation was monitored by flow cytometry (Fig. 3B). We noticed significantly reduced levels of chromatin-bound RPA in CtIP-F728E-Y736E-complemented cells compared with CtIP-WT-complemented cells (Fig. 3C,D), suggesting that expression of CtIP-F728E-Y736E may impair DNA2-dependent end resection in vivo.

However, RPA focus formation is a low-resolution technique to measure DNA end resection, as it does not retrieve quantitative data about the length of resected DNA. Consequently, we used a qPCR-based assay to quantify resection at two specific distances away from an AsiSI restriction enzyme-induced DSB to gain insights into the efficacy of both short- and long-range resection (Fig. 3E; Zhou et al. 2014). *EXO1*$^{-/-}$ DIvA cells were depleted of endogenous CtIP with siRNA and simultaneously transfected with siRNA-resistant FLAG-tagged CtIP-expressing variants (Fig. 3F; Supplemental Fig. S3F). Depletion of endogenous CtIP resulted in a strong decrease in end resection at locations both 200 and 740 bp away from the DSBs (Fig. 3G,H). The resection defect in the vicinity of the break (200 bp) could be largely rescued by expressing either wild-type CtIP or the F728E-Y736E mutant (Fig. 3G), indicating no major defects in short-range resection. In contrast, however, unlike wild-type CtIP, the CtIP-F728E-Y736E mutant failed to revert the DNA end resection defect 740 bp away from the break (Fig. 3H), in agreement with the hypothesis that CtIP-F728E-Y736E is not able to promote long-range resection by DNA2. Taken together, our experiments suggest that the point mutations disrupting DNA2–CtIP complex formation have negative effects on long-range DNA end resection by DNA2 while maintaining efficient short-range resection by the MRN complex, in agreement with our biochemical data.

Single-molecule analysis reveals that CtIP-F728E-Y736E inhibits resection also in EXO1$^{+/+}$ *cells*

The qPCR-based resection assay is limited to the analysis of resection at a site created by the endonuclease cut at a specific site of the genome. To measure resection genome-wide, we used the single-molecule analysis of resection tracks (SMART) technique (Huertas and Cruz-García 2018). To this point, U2OS cells were treated with either BrdU or CldU for 24 h to mark just one of the strands of the DNA. After inducing DNA damage and DSBs with 10 Gy of ionizing radiation (IR), DNA ends were resected, exposing either the BrdU or CldU epitopes in ssDNA. Upon hybridization with the corresponding antibody, the length of the resected tracks can be visualized (Supplemental Fig. S4A), thus allowing measurement of the extent of DNA resection (Fig. 4A; Supplemental Fig. S4B). Using this technique, we observed a significant decrease in the span of DNA resection tracks when the CtIP-F728E-Y736E mutant was overexpressed (Fig. 4B; Supplemental Fig. S4C), indicating a dominant-negative effect of CtIP-F728E-Y736E in resection. We note that the experiment was carried out in *EXO1*$^{+/+}$ cells without depleting endogenous CtIP. The fact that we observed resection impairment in CtIP-F728E-Y736E cells in an otherwise wild-type background (in the presence of EXO1) further supports the physiological relevance of the CtIP–DNA2 interplay in long-range resection.

CtIP-F728E-Y736E inhibits single-strand annealing and causes sensitivity to DNA damage

To further test the functional consequence of the impaired resection in the CtIP-F728E-Y736E mutant cells, we monitored single-strand annealing (SSA), which is a DSB repair pathway that relies on extended resection of DNA between two repeated sequences. Following an I-SceI-induced DSB, resection of a 2.7-kb-long DNA sequence, and annealing, a functional *GFP* gene is restored (Fig. 5A,B). As SSA relies on extended resection, it is often used as a reliable readout of physiological DNA end resection efficacy. Using *EXO1*$^{-/-}$ U2OS cells with the SA-GFP reporter (Stark et al. 2004), we tested how the expression of CtIP-F728E-Y736E complemented the loss of endogenous CtIP (Supplemental Figs. S3A, S5A). As anticipated, CtIP depletion resulted in a strong reduction of SSA (Fig. 5C). Importantly, complementation with the CtIP-F728E-Y736E mutant caused only a small increase in

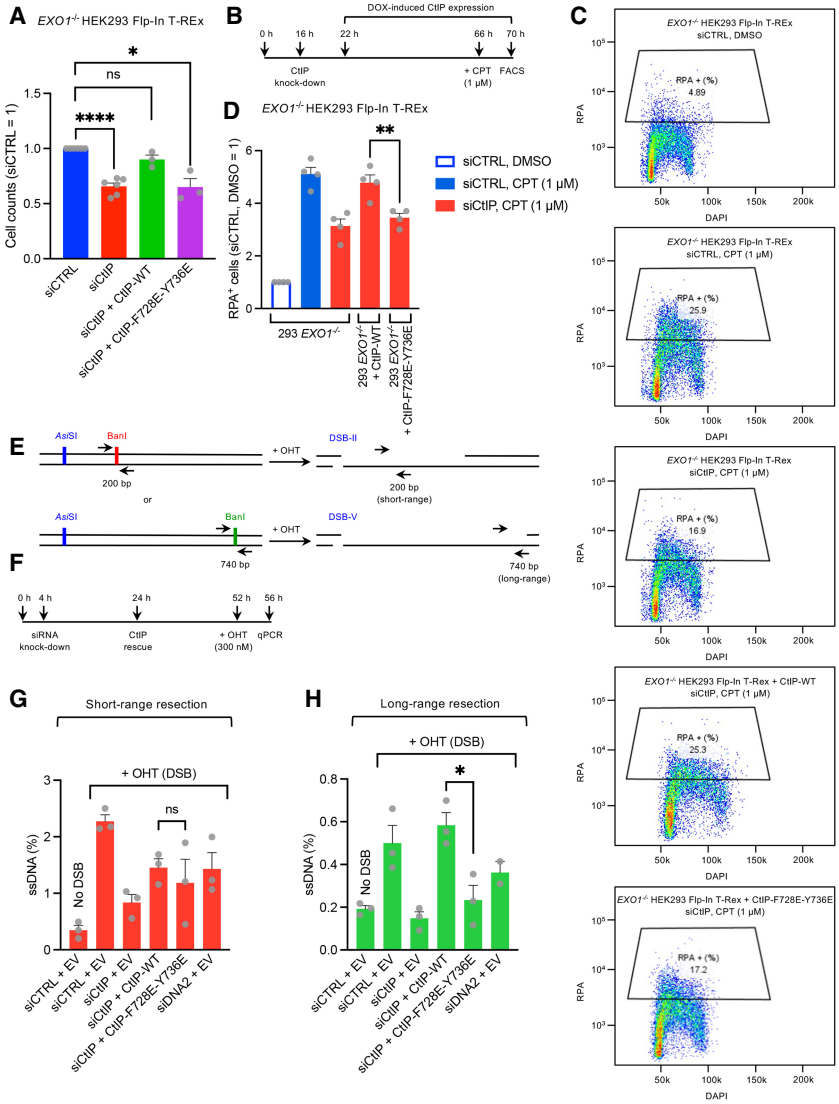

Figure 3. The CtIP-F728E-Y736E mutant inhibits DNA2-dependent long-range resection in cells. (*A*) Quantification of cell counts after normalizing to siCTRL and no doxycycline (DOX) in parental or wild-type CtIP-expressing or CtIP-F728E-Y736E-expressing *EXO1*$^{-/-}$ HEK293 Flp-In T-REx cells. $n \geq 3$; error bars indicate SEM. (****) $P < 0.0001$, (ns) $P > 0.05$ (not significant), (*) $P < 0.05$, two-tailed *t*-test. (*B*) Timeline of the chromatin-bound RPA detection assay in CtIP-expressing *EXO1*$^{-/-}$ HEK293 Flp-In T-REx cells after CPT treatment. (*C*) Representative flow cytometry plots of CtIP-expressing *EXO1*$^{-/-}$ HEK293 Flp-In T-REx cells treated with siCTRL or siCtIP followed by doxycycline-mediated overexpression of the indicated CtIP variant. Plots show the percentage of RPA^{+} cells upon mock (DMSO) or CPT treatment. (*D*) Quantitation of RPA^{+} cells from experiments such as shown in *C*. $n = 4$; error bars indicate SEM. (**) $P < 0.01$, two-tailed *t*-test. (*E*) Schematic of the qPCR reaction in *EXO1*$^{-/-}$ DIvA (AsiSI-ER-U2OS) cells upon DSB induction at the indicated AsiSI sites (DSB-II or DSB-V) with 4-hydroxytamoxifen (OHT). DNA end resection was monitored at sites either 200 or 740 bp away from the indicated DSBs. Arrows indicate the position of the PCR primers. (*F*) Timeline of the qPCR-based DNA end resection assay in *EXO1*$^{-/-}$ DIvA cells. (*G*) Quantification of the qPCR-based DNA end resection efficacy monitored at a site 200 bp away from the 4-hydroxytamoxifen (OHT)-induced DSB. $n = 3$; error bars indicate SEM. (ns) $P > 0.05$ (not significant), two-tailed *t*-test. EV, empty vector. (*H*) Quantification of the qPCR-based DNA end resection efficacy monitored at a site 740 bp away from the 4-hydroxytamoxifen (OHT)-induced DSB. $n \geq 2$; error bars indicate SEM. (*) $P < 0.05$, two-tailed *t*-test. EV, empty vector.

SSA compared with complementation with wild-type CtIP, suggesting that CtIP-F728E-Y736E is not fully functional in long-range resection and hence SSA. Moreover, complementation with CtIP-F728E-Y736E resulted in SSA defects comparable with siDNA2-treated cells (Fig. 5C), in agreement with the model that the CtIP-F728E-Y736E mutant impairs the DNA2-mediated long-range DNA end resection pathway. In contrast, CtIP-F728E-Y736E did not impair DSB repair in U2OS-EJ2 reporter cells, which primarily score for alternative end joining (AltEJ and MMEJ), which does not rely on extensive DNA resection (Fig. 5D,E; Supplemental Fig. S5B).

To assess how the CtIP-F728E-Y736E variant affects cellular sensitivity to DNA damage, we next used the topoisomerase I inhibitor camptothecin (CPT), which causes replication-associated DSBs and hence preferentially kills CtIP-depleted cells (Sartori et al. 2007; Nakamura et al. 2010). Using the two different cell lines, *EXO1*$^{-/-}$ HEK293 Flp-In T-REx and *EXO1*$^{-/-}$ U2OS-derived DIvA, we observed that CtIP depletion resulted in cellular sensitivity to CPT, as reported previously (Sartori et al. 2007). Expression of wild-type CtIP resulted in increased cell survival, while expression of CtIP-F728E-Y736E did not (Fig. 5F,G; Supplemental Fig. S5C). We conclude that the long-range resection defects observed in CtIP-F728E-Y736E cells negatively impact SSA efficacy and cause sensitivity to DSB-inducing drugs.

Phosphorylation of CtIP at S723 by PLK1 down-regulates resection through disrupting the interplay with DNA2

As described previously, CDK1/Aurora A facilitate phosphorylation of CtIP by PLK1 (Wang et al. 2018). A phosphorylation-mimicking CtIP-3E mutant (T693E, S723E, and T731E) exhibited impaired long-range resection, while error-prone MMEJ, which does not require long-range resection, was instead enhanced (Wang et al. 2018). The underlying mechanism remained unknown. We noted that the residues subject to phosphorylation are located within or near the DNA2 interaction patch in CtIP, identified here (Fig. 1A–C). We next set out to define the importance of these CtIP phosphorylation sites

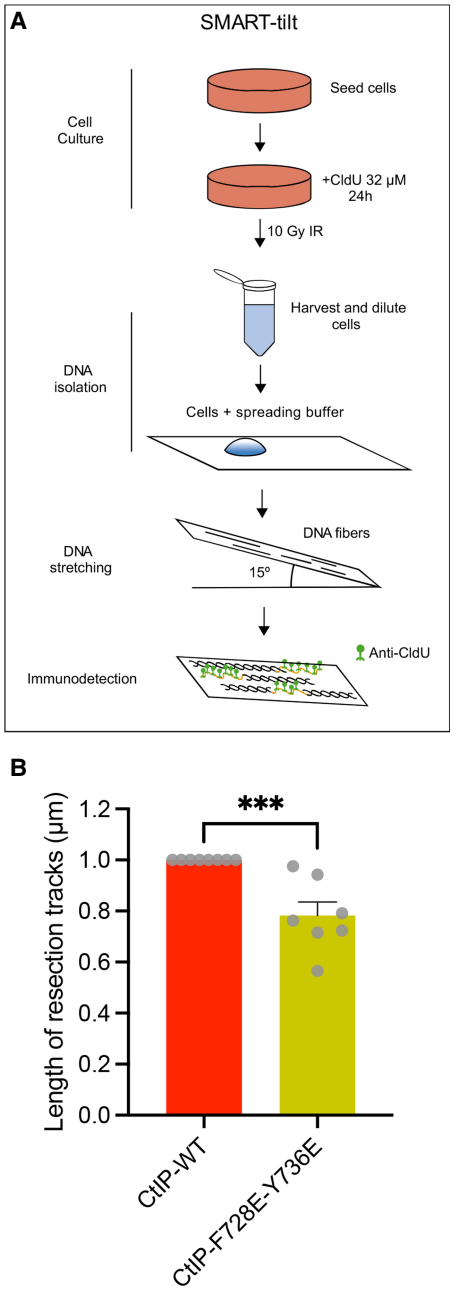

Figure 4. Single-molecule analysis reveals that CtIP-F728E-Y736E inhibits resection also in *EXO1*$^{+/+}$ cells. (*A*) A schematic representation of the SMART protocol using the tilting SMART assay. (*B*) Quantification of the length of ssDNA fibers. Cultures were irradiated at 10 Gy and harvested after 1 h. The values are normalized to CtIP-WT. $n = 7$; error bars indicate SEM. (***) $P < 0.001$, two-tailed *t*-test. The presented data were pooled from experiments with BrdU, as shown in Supplemental Figure S4B, and CldU labeling, as shown in *A*.

for the interplay of CtIP with DNA2. We expressed and purified recombinant nonphosphorylatable S723A or phosphorylation-mimetic S723E pCtIP variants (Supplemental Fig. S6A), together with the previously described 3E (T693E, S723E, and T731E) (Wang et al. 2018) and CtIP-3A (T693A, S723A, and T731A) mutants (Supplemental Fig. S6B), and analyzed them for their ability to stimulate DNA2.

We observed that pCtIP-S723A and pCtIP-S723E, and similarly pCtIP-3A and pCtIP-3E, were strongly impaired in the stimulation of long-length ssDNA degradation by DNA2 (Fig. 6A,B). Both the alanine and the phosphomimetic substitution mutants were compromised, demonstrating that the integrity of the respective residues in pCtIP is very important for the stimulation of DNA2. Accordingly, the pCtIP mutants were less efficient in the stimulation of the DNA2 ATPase (Supplemental Fig. S6C,D). We noted that the pCtIP variants could not bind DNA2 as efficiently as pCtIP wild type (Fig. 6C–E). In contrast, pCtIP-S723A and pCtIP-S723E stimulated the endonuclease of MRN almost as well as wild-type pCtIP (Supplemental Fig. S6E,F), suggesting that pCtIP phosphorylation at S723 primarily affects long-range resection, in agreement with cellular data (Wang et al. 2018). As expected for a mutant with a defect in DNA2 stimulation, CtIP-S723A-overexpressing cells showed an impaired DNA resection phenotype, since a reduction in DNA resection length could be observed compared with CtIP wild-type-overexpressing cells (Supplemental Fig. S6G–I).

Given that PLK1 was proposed to phosphorylate CtIP in vivo (Wang et al. 2018), we asked whether recombinant PLK1 was able to directly phosphorylate pCtIP and affect its function in vitro. As previously stated, we used pCtIP prepared with phosphatase inhibitors, as nonphosphorylated CtIP is largely aggregated and cannot be efficiently purified. Therefore, our pCtIP preparation already has some, but not all, phosphorylation sites modified (Anand et al. 2016, 2019). Nevertheless, we observed that recombinant PLK1 further phosphorylated pCtIP in a radioactive kinase assay (Fig. 6F). Moreover, wild-type pCtIP was more efficiently in vitro phosphorylated compared with the pCtIP-S723A or pCtIP-3A mutants (Fig. 6F), showing that S723 is one of the main targets of PLK1 in CtIP, as suggested previously (Wang et al. 2018). Having established efficient in vitro phosphorylation of pCtIP by PLK1, we used the modified pCtIP protein to test its activity as a cofactor in short- and long-range resection. PLK1-treated pCtIP was significantly impaired in its ability to stimulate DNA degradation by DNA2 (Fig. 6G,H). In contrast, PLK1-treated pCtIP was indistinguishable from mock-treated pCtIP in the stimulation of the MRN endonuclease activity (Fig. 6I; Supplemental Fig. S6J). Taken together, these experiments explain how PLK1-mediated phosphorylation of CtIP inhibits long-range resection (Wang et al. 2018) and further support the physiological relevance of CtIP and DNA2 interplay (Fig. 7).

Discussion

CtIP functions as an activator of the MRN complex to initiate short-range DNA end resection (Anand et al. 2016; Deshpande et al. 2016). More recently, in vitro studies revealed that CtIP also controls the DNA2 translocase and the BLM helicase, which function in resection

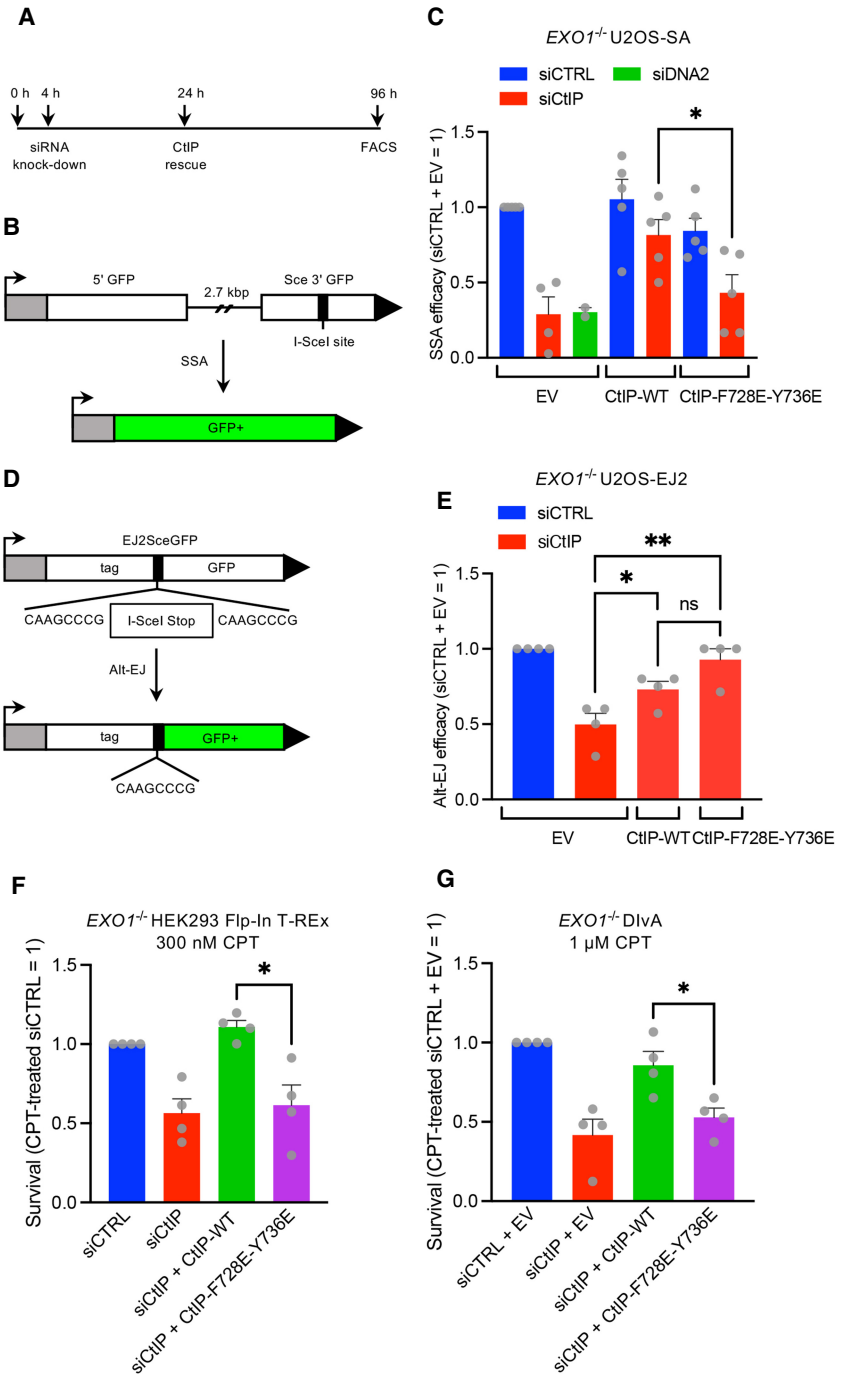

Figure 5. CtIP-F728E-Y736E inhibits single-strand annealing and causes sensitivity to DNA damage. (*A*) Timeline of the GFP-based DSB reporter assays in *EXO1*$^{-/-}$ U2OS cells. (*B*) Schematic of the single-strand annealing assay in *EXO1*$^{-/-}$ U2OS-SA cells. (*C*) Quantification of the single-strand annealing efficacy after normalizing to siCTRL + EV. $n \geq 2$; error bars indicate SEM. (*) $P < 0.05$, two-tailed *t*-test. (EV) Empty vector. (*D*) Schematic of the microhomology-mediated end-joining repair assay in *EXO1*$^{-/-}$ U2OS-EJ2 cells. (*E*) Quantification of the microhomology-mediated end-joining efficacy after normalizing to siCTRL + EV. $n = 4$; error bars indicate SEM. (*) $P < 0.05$, (**) $P < 0.001$, (ns) $P > 0.05$ (not significant), two-tailed *t*-test. (EV) Empty vector. (*F*) Quantitation of clonogenic cell survival upon acute treatment with 300 nM CPT for 2 h in *EXO1*$^{-/-}$ HEK293 Flp-In T-REx cells, where endogenous CtIP was mock-depleted (siCTRL) or depleted (siCtIP) and either wild-type CtIP or CtIP-F728E-Y736E expression was induced with doxycycline. The values are normalized to siCTRL treated with 300 nM CPT. $n = 4$; error bars indicate SEM. (*) $P < 0.05$, two-tailed *t*-test. (*G*) Quantitation of clonogenic cell survival upon acute treatment with 1 µM CPT for 1 h in *EXO1*$^{-/-}$ DIvA cells, where endogenous CtIP was mock-depleted (siCTRL) or depleted (siCtIP) and complemented with the indicated CtIP variant. The values are normalized to siCTRL + EV treated with 1 µM CPT. $n = 4$; error bars indicate SEM. (*) $P < 0.05$, two-tailed *t*-test. (EV) Empty vector.

downstream from MRN (Daley et al. 2017; Ceppi et al. 2020). In addition, CtIP inhibits EXO1 5′ → 3′ exonuclease activity in vitro (Eid et al. 2010). It was demonstrated that CtIP promotes the DNA degradation by DNA2 via the stimulation of DNA2 translocase activity, which likely accelerates the rate by which DNA gets fed into the DNA2 nuclease domain (Ceppi et al. 2020). However, it was not clear to what extent such interplay is relevant for DNA end resection in cells. Particularly, in the context of replication stress, CtIP was instead shown to restrict pathological DNA2 activity (Przetocka et al. 2018). Therefore, the interplay of DNA2 and CtIP in a cellular setting was not obvious and required careful examination. To this point, we set out to identify a separation-of-function CtIP mutant that would be proficient in stimulating MRN and hence unaffected in short-range resection but specifically deficient in activating DNA2.

Here, we adopted a combined evolutionary and structural modeling approach to predict the mode of interaction between CtIP region 690–740 in CtIP orthologs and DNA2 (Ceppi et al. 2020). We designed the CtIP-F728E-Y736E mutant, which activates MRN similarly to wild

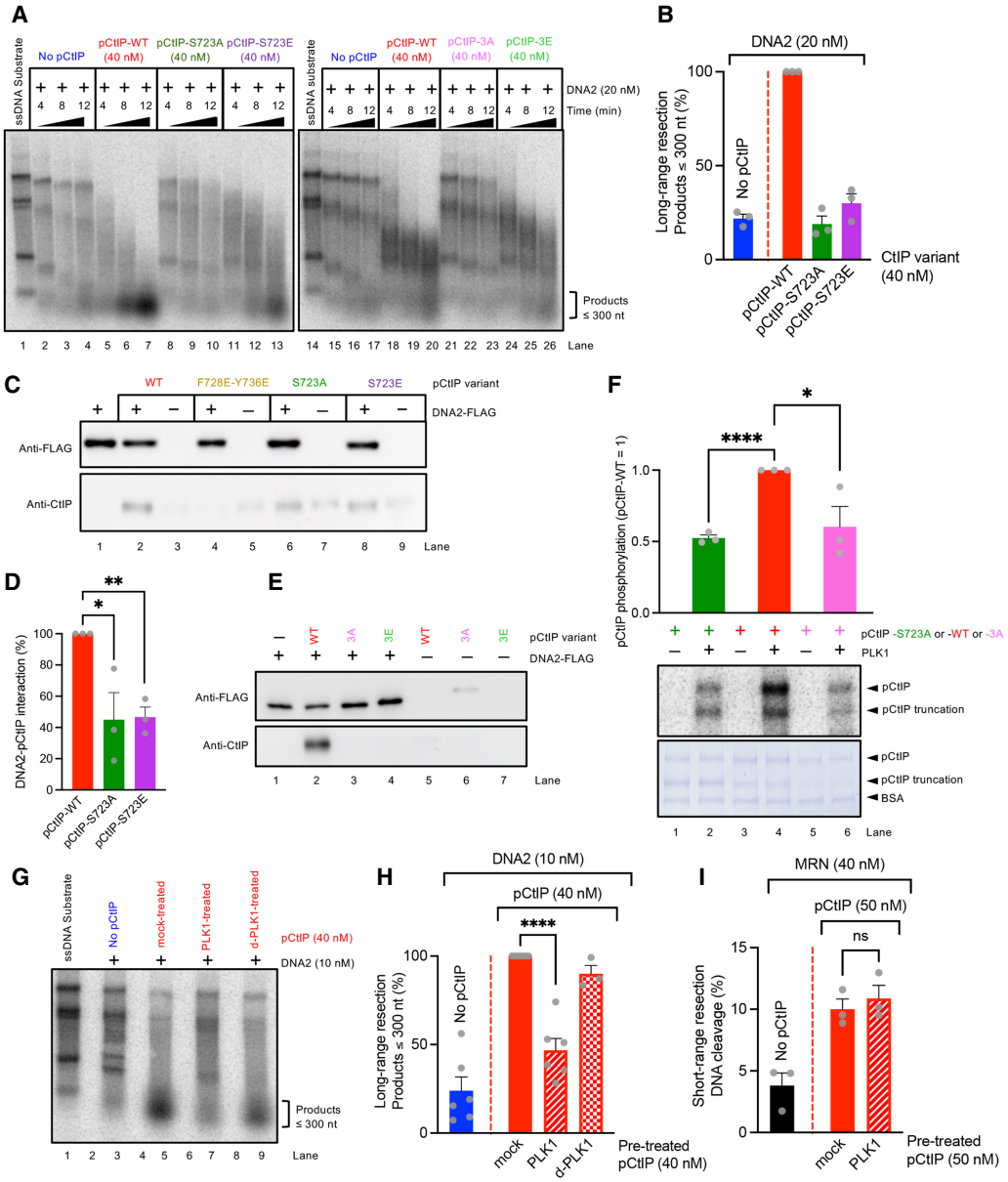

Figure 6. Phosphorylation of CtIP at S723 by PLK1 down-regulates DNA2-dependent resection. (*A*) Degradation of ssDNA fragments of various length by 20 nM DNA2 without or with 40 nM indicated pCtIP variant in the presence of 864 nM RPA. (*B*) Quantitation of small degradation products (≤300 nt) from experiments such as shown in *A* after 8 min. $n = 3$; error bars indicate SEM. (*C*) A representative DNA2 interaction assay with the indicated pCtIP variants (see cartoon in Fig. 2C). DNA2-FLAG was immobilized on M2 anti-FLAG affinity resin. The Western blot was performed with anti-FLAG and anti-CtIP antibodies. (*D*) Quantitation of the DNA2–pCtIP interaction from experiments such as shown in *C*. $n = 3$; error bars indicate SEM. (*) $P < 0.05$, (**) $P < 0.01$, two-tailed *t*-test. (*E*) DNA2 interaction assays with indicated pCtIP variants (see cartoon in Fig. 2C). DNA2-FLAG was immobilized on M2 anti-FLAG affinity resin. The Western blot was performed with anti-FLAG and anti-CtIP antibodies. (*F*) In vitro phosphorylation of pCtIP by PLK1. Purified pCtIP-WT, pCtIP-S723A, and pCtIP-3A were incubated in an in vitro kinase assay with PLK1. (*Top*) Quantification. The radioactive signal is normalized to PLK1-treated pCtIP-WT. $n = 3$; error bars indicate SEM. (****) $P < 0.0001$, (*) $P < 0.05$, two-tailed *t*-test. (*Bottom*) Coomassie-stained proteins after PAGE. (*Middle*) Autoradiograph of the identical gel. (*G*) Degradation of ssDNA fragments of various lengths by 10 nM DNA2 without or with 40 nM pCtIP either mock-treated or prephosphorylated by either PLK1 or heat-inactivated d-PLK1 in the presence of 864 nM RPA. (*H*) Quantitation of small degradation products (≤300 nt) from experiments such as shown in *G*. $n \geq 3$; error bars indicate SEM. (****) $P < 0.0001$, two-tailed *t*-test. (*I*) Quantitation of endonucleolytic DNA cleavage from experiments such as shown in Supplemental Figure S6J. $n = 3$; error bars indicate SEM. (ns) $P > 0.05$ (not significant), two-tailed *t*-test.

type but is deficient in physical and functional interactions with DNA2. Our structural model allowed us to speculate how the specific residues might be able to bind and activate the DNA2 translocase (Fig. 1B). F728 would be important for stable anchoring of CtIP to DNA2, while Y736 might rather modulate the way

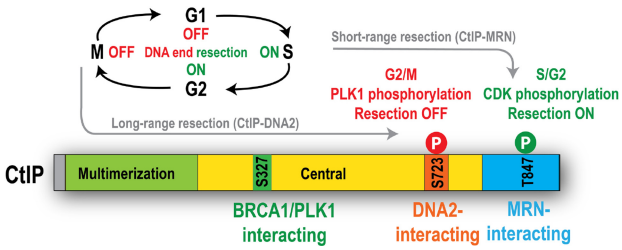

Figure 7. Model for CtIP-mediated regulation of DNA2-dependent long-range DNA end resection. A schematic depicting the role of pCtIP in the regulation of DNA2-dependent long-range resection. CDK phosphorylates CtIP early in the cell cycle and activates DNA end resection at the S/G2 stage, when sister chromatids are available as templates for repair. Instead, at M phase, PLK1 phosphorylates CtIP at S723, thus negatively regulating DNA2-dependent long-range end resection.

nucleotides interact with DNA2 in a yet unknown manner. One speculative model would be that CtIP-Y736 specifically disturbs the interaction of ADP in the DNA2 nucleotide binding site, playing the role of an ADP exchange factor to increase the turnover of the enzyme, consistent with CtIP's ability to stimulate DNA2 ATPase-driven motor activity. The evolutionary properties indicate that the interaction between CtIP and DNA2 through this motif would be restricted to vertebrate species. Indeed, previous data showed that the stimulation of the DNA2 translocase activity by CtIP could not be recapitulated in the yeast system and was indeed dependent on the CtIP region that is absent in the yeast homolog Sae2 (Ceppi et al. 2020).

Using a variety of complementary cellular assays in various genetic backgrounds, we observed that CtIP-F728E-Y736E mutant-expressing cells show decreased accumulation of chromatin-bound RPA upon DSB induction and, consequently, decreased survival (Figs. 3–5). Using assays to monitor DNA end resection at various positions in the human genome, we observed that resection in CtIP-F728E-Y736E-expressing cells was not affected when monitoring resection of a site in the vicinity of the DNA break. However, a clear resection defect was observed when a position at a greater distance from the break was analyzed, supporting our biochemical data showing that the F728E and the Y736E mutations affect specifically the interplay of CtIP and DNA2 in long-range resection. The majority of the cellular experiments were carried out in the *EXO1*-deficient background, but a clear defect of DNA end resection genome-wide was also observed in *EXO1*-proficient cells upon overexpression of the CtIP-F728E-Y736E variant. Therefore, we conclude that disrupting the interaction between DNA2 and CtIP in cells results in defects in DNA end resection.

The identified DNA2-interacting patch in CtIP includes a previously recognized PLK1 target site (Wang et al. 2018). Specifically, in nocodazole-arrested mitotic cells, the CtIP-3E mutant (T693E, S723E, and T731E) was shown to inhibit extended end resection and instead promote MMEJ (Wang et al. 2018). However, mechanistic insights about how PLK1-mediated phosphorylation of CtIP inhibits the long-range resection were missing; in fact, it was not known how CtIP promotes extended resection at all. We showed that the integrity of S723 is critical for the stimulation of DNA2, as both S723A and S723E mutations failed to promote DNA2 (Fig. 6). In contrast to the nearly complete disruption of the functional interplay, the two substitution mutations in CtIP also reduced physical interaction with DNA2 but to a lesser extent. The structural model predicts contacts between CtIP-S723 and DNA2-K616 and DNA2-H613 (Fig. 1C). It is possible that phosphorylated S723 may induce allosteric conformational changes in the DNA2 helix 614–624 (containing K616), likely affecting nucleotide binding properties, since the DNA2 G625 backbone directly contacts the N6 atom of the nucleotide base. Such changes may explain the disruption of the ATP hydrolysis-dependent stimulation of DNA2 nuclease by the CtIP-S723 mutants without strongly affecting the protein–protein interaction. Nevertheless, more insights are needed to understand the regulation of DNA2 and CtIP interplay specifically by S723 phosphorylation on the atomic level.

Phosphorylation of CtIP early in the cell cycle by CDK activates DNA end resection and hence homologous recombination at the cell cycle stage (S/G2), when sister chromatids are available as templates for homology-directed repair (Ira et al. 2004; Huertas et al. 2008; Huertas and Jackson 2009). CDK phosphorylation activates additional components of the resection machinery (Chen et al. 2011; Ferretti et al. 2013), and CtIP is further activated by ATM- and DNA damage-dependent activity in response to DSBs (Peterson et al. 2013; Deshpande et al. 2020). In contrast to the activation of resection by phosphorylation, much less is known about what terminates resection. As chromatin remodeling in the vicinity of DSBs is needed for efficient resection (Chen et al. 2012; Costelloe et al. 2012; Dong et al. 2014; Kollárovič et al. 2020), there may be a physical limit to how far resection can go, governed by the extent of chromatin remodeling. Additionally, pCtIP may be targeted for degradation (Ferretti et al. 2016; Li et al. 2020; Han et al. 2021), or pCtIP may be dephosphorylated (Isobe et al. 2021). Phosphorylation of RPA was described to inhibit long-range resection dependent on BLM (Soniat et al. 2019). The mechanism uncovered here—inhibitory phosphorylation of CtIP—goes along the same lines, showing yet another mode of negative regulation of long-range end resection (Fig. 7). As PLK1 activity peaks late in the cell cycle at M phase, PLK1-dependent modification of CtIP at S723 would disrupt DNA2-dependent resection and hence HR initiation at a cell cycle stage when it is no longer desirable while still allowing alternative repair pathways such as MMEJ. Notably, PLK1-mediated phosphorylation of BLM instead enhances its double-Holliday junction dissolution activity (Balbo Pogliano et al. 2022). Late in the cell cycle, PLK1 thus likely orchestrates a switch to limit initiation of recombination (resection) while promoting completion of recombination (dissolution) to guarantee flawless separation of genetic material during subsequent cellular division.

Materials and methods

Sequence analysis and modeling of the interaction between human DNA2 and CtIP

Orthologs of DNA2 and CtIP were retrieved using three iterations of HHblits (Steinegger et al. 2019) on the UniProt30 database (Mirdita et al. 2017). Homologs sharing <20% and 30% for CtIP and DNA2, respectively, and a coverage <30% and 50% for CtIP and DNA2, respectively, were discarded. In case several homologs belonged to the same species, only the one sharing highest sequence identity with the query was kept. Full-length sequences of the selected homologs were then retrieved and realigned with mafft (Katoh and Standley 2013). To model the structure of the DNA2–CtIP complex, MSAs of DNA2 and CtIP (645–753) containing 2124 and 821 homolog sequences of DNA2 and CtIP, respectively, were concatenated, resulting in 1169 aligned positions. When homologs of the subunits belonged to the same species, they were aligned in a paired manner; otherwise, they were left unpaired. The concatenated MSA was used as input to run five independent simulations of the AlphaFold2 algorithm with six iterations each (Jumper et al. 2021), generating five structural models using a local version of the ColabFold interface (Mirdita et al. 2022), trained on the multimer data set (Evans et al. 2022) on a local HPC equipped with NVIDIA Ampere A100 80Go GPU cards. The best models of each of the five runs converged toward similar conformations. They reached high confidence and quality scores with pLDDTs in the range [82.9, 83.7] and pTMscore in the range [0.834, 0.84]. The model with the highest pTMscore was relaxed using Rosetta relax protocols to remove steric clashes (Leman et al. 2020) with strong backbone constraints (standard deviation of 0.5 Å for the atomic positions) and was used for structural analysis. Surface conservation was calculated for DNA2 homologs using the Rate4Site algorithm (Pupko et al. 2002) on the ConSurf server (Ashkenazy et al. 2016). Figures were prepared using Jalview for sequences (Waterhouse et al. 2009) and PyMOL for structures (the PyMOL molecular graphics system, version 2.0, Schrödinger, LLC). The model is available in ModelArchive at https://modelarchive.org/doi/10.5452/ma-b36a2.

Chromatin-bound RPA assay

The sequences of the two crRNAs targeting *EXO1* used in this study are listed in Supplemental Table S1. The sequences of all primers used in this study are listed in Supplemental Table S2. One day before transfection, stable *EXO1*$^{-/-}$ HEK293 Flp-In T-REx cells were plated in 2 mL of antibiotic-free medium in six-well plates such that they would be 40%–50% confluent at the time of transfection. The next day, cells were transfected with 20 pmol of siRNA and 7.2 µL of RNAiMAX (Invitrogen) in 500 µL of Opti-MEM (Gibco) and cultured for 5 h before the addition of 0.5 ng/mL doxycycline to induce the expression of wild-type CtIP or the F728E-Y736E mutant. Forty-four hours after the addition of doxycycline, cells were treated with 1 µM CPT (Sigma) for 4 h to induce DNA lesions. Cells were then trypsinized, washed with cold PBS, and permeabilized with 0.2% Triton X-100 in PBS for 7 min. All washing steps were conducted by spinning cells at 660*g* for 4 min. After permeabilization, the cells were washed with 0.1% BSA in PBS, fixed with Cytofix/Cytoperm buffer (BD), and incubated for 15 min at room temperature in the dark. Cells were then washed with 0.1% BSA in PBS and incubated with RPA primary antibody (1:200; Calbiochem NA19L) for 1 h at room temperature in the dark. Samples were washed again with 0.1% BSA in PBS and incubated with a fluorescent secondary goat antimouse Alexa Fluor 647 antibody (1:200; Invitrogen A21236) for 30 min at room temperature in the dark. Finally, cells were washed with 0.1% BSA in PBS; resuspended in 0.3 mL of PBS with 0.02% sodium azide (Sigma), 250 µg/mL RNase A (Sigma), and 2 µg/mL DAPI (Sigma); and then incubated for 30 min at 37°C in the dark. The fraction of RPA-positive cells was then scored on a LSR Fortessa flow cytometer (BD) and quantified using FlowJo software (BD) (Forment et al. 2012). The sequences of all siRNAs used in this study are listed in Supplemental Table S3.

qPCR-based end resection assay

The sequences of the two crRNAs targeting *EXO1* used in this study are listed in Supplemental Table S1. *EXO1*$^{-/-}$ DIvA (AsiSI-ER-U2OS) cells were plated in 2 mL of antibiotic-free media in six-well plates such that they would be 40%–50% confluent at the time of transfection. Four hours after plating, cells were transfected with 20 pmol of siRNA and 7.2 µL of RNAiMAX (Invitrogen) in 400 µL of Opti-MEM (Gibco) and cultured for 20 h. Cells were then complemented with 2.4 µg of siRNA-resistant pcDNA3.1 empty vector or vector expressing either wild-type CtIP or CtIP-F728E-Y736E. Forty-eight hours after transfection, cells were treated with 300 nM (*Z*)-4-hydroxytamoxifen (Sigma) or mock-treated for 4 h. Cells were then washed twice, trypsinized, and pelleted by centrifugation at 200*g* for 5 min. Genomic DNA was isolated using a DNeasy kit (Qiagen) with RNase A treatment during lysis. Next, 500 ng of genomic DNA was treated with 5 U of RNase H (New England Biolabs) for 15 min at 37°C and heat-inactivated for 20 min at 65°C. RNase H-treated genomic DNA (150 ng) was digested with 16 U of BanI (New England Biolabs) or mock-digested overnight at 37°C and then heat-inactivated for 20 min at 65°C. Finally, 2 ng of digested or mock-digested genomic DNA was used in a 10-µL qPCR reaction (PerfeCTa SYBR Green fast mix, Quanta Bio) with 300 nM primers flanking the BanI sites at 200 bp from the DSB-II AsiSI site or 740 bp from the DSB-V AsiSI site, respectively. The sequences of all primers used in this study are listed in Supplemental Table S2. The qPCR reactions were run using MicroAmp Fast 96-well optical plates and adhesive film (Applied Biosystems) on a QuantStudio 3 real-time PCR system (Applied Biosystems) using the standard SYBR Green program according to the manufacturer's instructions. The percentage of ssDNA generated for each sample was calculated in Microsoft Excel using the following equation: percent ssDNA = 1/[POWER(2,Ct digested sample – Ct nondigested sample – 1) + 0.5] × 100 (Zhou et al. 2014).

GFP-based reporter assays

The sequences of the two crRNAs targeting *EXO1* used in this study are listed in Supplemental Table S1. *EXO1*$^{-/-}$ U2OS-SA or U2OS-EJ2 cells (0.45×10^5 cells) were seeded in 0.5 mL of antibiotic-free media in 24-well plates; 3 h later, cells were transfected with 6 pmol of siRNA and 1 µL of RNAiMAX (Invitrogen) in 100 µL of Opti-MEM (Gibco) and cultured for 20 h. The cells were transfected for 5 h with 0.4 µg of I-SceI (pCBASce) and 0.2 µg of empty pcDNA3.1 vector, pcDNA3.1-CtIP-WT-2XFLAG vector, or pcDNA3.1-CtIP-F728E-Y736E-2XFLAG vector using Lipofectamine 2000 transfection reagent (Invitrogen) in 100 µL of Opti-MEM. After 5 h, cells were washed and cultured in complete medium for 3 d to allow for the repair of the DSB. Cells were then scored for the percentage of GFP-positive cells on a LSR Fortessa flow cytometer (BD) (Stark et al. 2004). The sequences of all siRNAs used in this study are listed in Supplemental Table S3.

Cell proliferation and viability assays

The sequences of the two crRNAs targeting *EXO1* used in this study are listed in Supplemental Table S1. To evaluate cell growth, 300,000 stable *EXO1*$^{-/-}$ HEK293 Flp-In T-REx cells were seeded in a six-well plate and 24 h later were transfected with the indicated siRNA as described for the chromatin-bound RPA assays. Twenty-four hours after transfection, cells were counted and reseeded in six-well plates (300,000 cells/well) in the presence of doxycycline to induce the expression of wild-type CtIP or the F728E-Y736E mutant. Forty-eight hours later, cells were counted again. Results are shown as cell counts normalized for the siCTRL control.

Clonogenic survival assay

The sequences of the two crRNAs targeting *EXO1* used in this study are listed in Supplemental Table S1. Stable *EXO1*$^{-/-}$ HEK293 Flp-In T-REx cells were seeded in 24-well plates such that they would be 40% confluent at the time of transfection. The next day, cells were transfected with 6 pmol of siRNA and 1 µL of RNAiMAX (Invitrogen) in 100 µL of Opti-MEM (Gibco) and cultured for 5 h before reseeding at low density in the presence of 0.5 ng/mL doxycycline to induce the expression of wild-type CtIP or the F728E-Y736E mutant. Forty-eight hours after the addition of doxycycline, 1000 cells per dish were seeded in 10-cm dishes in duplicate per each condition. Cells were allowed to adhere for 6 h in drug-free media and then treated with the indicated concentrations of CPT (Sigma) for 2 h. The cells were then washed and fed with drug-free media. Colonies were allowed to grow for 7–10 d. Colonies were fixed with cold 100% methanol and stained with 0.5% crystal violet in 20% methanol. *EXO1*$^{-/-}$ DIvA (AsiSI-ER-U2OS) cells were seeded in 12-well plates such that they would be 40% confluent at the time of transfection. The next day, cells were transfected with 10 pmol of the indicated siRNA and 3.6 µL of RNAiMAX (Invitrogen) in 200 µL of Opti-MEM (Gibco) and cultured for 20 h. The cells were transfected for 5 h with 1.2 µg of empty pcDNA3.1 vector, pcDNA3.1-CtIP-WT-2XFLAG vector, or pcDNA3.1-CtIP-F728E-Y736E-2XFLAG vector using Lipofectamine 2000 transfection reagent (Invitrogen) in 200 µL of Opti-MEM. After 5 h, the cells were washed and cultured in complete medium until the following morning. One-thousand-five-hundred cells per dish were seeded in 10-cm dishes in duplicate per each condition. Cells were allowed to adhere for 6 h in drug-free media and then treated with the indicated concentrations of CPT (Sigma) for 1 h. For experiments with MRE11 inhibitors, cells were treated with 50 µM PFM03 (Sigma) and 50 µM PFM39 (Sigma) for 30 min prior to CPT addition. The cells were then washed and fed with drug-free media. Colonies were allowed to grow for 7–10 d, fixed, and stained as described above.

Immunoblotting

For the immunoblot analysis, the cells were transfected as described for the corresponding in vivo assays in six-well plates and, 48 h after transfection, lysed in RIPA buffer containing 50 mM Tris-HCl (pH 8.0), 150 mM NaCl, 1% NP-40, 0.5% sodium deoxycholate, 0.1% sodium dodecylsulfate (SDS), 1% protease inhibitor cocktail (Sigma), and 1 mM PMSF. Cell lysates were incubated for 30 min on ice with occasional vortexing and then cleared by centrifugation at 12,000*g* for 5 min at 2°C. Proteins in the cell extract were quantitated with DC protein assay (Bio-Rad) according to the manufacturer's instructions. Subsequent SDS-PAGE and Western blotting were performed using standard methods using the following antibodies and dilutions: anti-β-Actin (1:1000; Santa Cruz Biotechnology sc-47778), anti-β-Tubulin (1:1000; Santa Cruz Biotechnology sc-9104), anti-CtIP (1:1000; Santa Cruz Biotechnology sc-271339), and anti-EXO1 (1:1000; Abcam ab95068). Retrieved protein complexes following coimmunoprecipitation were boiled in SDS sample buffer and analyzed by SDS-PAGE, followed by immunoblotting using the following antibodies: anti-CtIP (1:250; Santa Cruz Biotechnology sc-271339), anti-DNA2 (1:500; Abcam ab96488), and anti-GAPDH (1:2000; Millipore MAB374).

Nuclease assays

Nuclease assays with 0.15 nM (in molecules) 3′-labeled Hind III digest of λ DNA were performed in 15-µL volume in 25 mM Tris-acetate (pH 7.5), 3 mM magnesium acetate, 1 mM ATP, 1 mM DTT, 0.1 mg/mL BSA (New England Biolabs), 1 mM phosphoenolpyruvate (PEP), and 80 U/mL pyruvate kinase (Sigma). Human RPA (864 nM) was included as indicated to saturate all ssDNA. Recombinant proteins were then added on ice, and the reactions were incubated for 8 min at 37°C. Reactions were stopped by adding 5 µL of 2% stop solution (150 mM EDTA, 2% sodium dodecyl sulfate, 30% glycerol, bromophenol blue) and 1 µL of 14–22 mg/mL proteinase K (Roche) and incubated for 10 min at 37°C. Samples were analyzed by 1% agarose gel electrophoresis. Gels were squeezed and dried on DE81 chromatography paper (Whatman), exposed to storage phosphor screens (GE Healthcare), and scanned by a Typhoon 9500 phosphorimager (GE Healthcare). Endonuclease assays with MRN and 15-µL volume of phosphorylated CtIP were performed in nuclease buffer containing 25 mM Tris-HCl (pH 7.5), 5 mM magnesium acetate, 1 mM manganese acetate, 1 mM ATP, 1 mM DTT, 0.25 mg/mL BSA, and 1 nM oligonucleotide-based DNA substrate (in molecules) (see Supplemental Table S4). Biotinylated DNA ends were blocked by adding 15 nM monovalent streptavidin (a kind gift from Mark Howarth, University of Oxford) and incubating the samples for 5 min at room temperature. The reactions were incubated for 2 h at 37°C, stopped by adding 0.5 µL of 0.5 M EDTA and 1 µL of 14–22 mg/mL proteinase K (Roche), and incubated for 30 min at 50°C. An equal amount of formamide dye (95% [v/v] formamide, 20 mM EDTA, bromophenol blue) was added, and samples were heated for 4 min at 95°C and separated on 15% denaturing polyacrylamide gels (ratio acrylamide:bisacrylamide 19:1; Bio-Rad). After fixing in a solution containing 40% methanol, 10% acetic acid, and 5% glycerol for 30 min, the gels were dried on 3-mm paper (Whatman) and analyzed as described above. Kinetic experiments with randomly labeled 2200-nt-long substrate (1 nM in molecules) were performed in 15-µL volume using the same buffer described for the λ/Hind III ssDNA substrate, except for the magnesium acetate, which was used at 2 mM final concentration. RPA (176 nM) was included to saturate all ssDNA. The reactions were assembled on ice and incubated for the indicated time at 37°C. Samples were then stopped as described above for the endonuclease assays and analyzed on 20% denaturing polyacrylamide gels. Fixing, drying, and analysis were performed as described above.

Recombinant protein interaction assays

To test for interactions between DNA2 and pCtIP variants, 6Xhis-DNA2-FLAG wild type or L623E-K636E-L640E mutant was expressed in *Sf*9 cells. Cells were lysed, and soluble extract containing DNA2 (bait) was bound to 50 µL of M2 anti-FLAG affinity resin (Sigma). The resin was washed with wash buffer 1 (50 mM Tris-HCl at pH 7.5, 300 mM NaCl, 10% glycerol, 1 mM PMSF, 0.5 mM β-mercaptoethanol, 0.1% NP40) and incubated

for 1 h at 4°C with 1 µg of the indicated recombinant purified pCtIP variant (prey) in IP buffer (25 mM Tris-HCl at pH 7.5, 0.5 mM DTT, 3 mM EDTA, 100 mM NaCl, 0.20 µg/µL BSA). The resin was then washed five times with wash buffer 2 (50 mM Tris-HCl at pH 7.5, 0.5 mM DTT, 3 mM EDTA, 80 mM NaCl, 0.1% NP40), and proteins were eluted with 70 µL of wash buffer 2 containing 150 ng/µL of 3XFLAG peptide (APExBIO). As a negative control, purified pCtIP variants were incubated with the resin that had not been bound to 6Xhis-DNA2-FLAG. The proteins in the eluate were analyzed by Western blotting using anti-FLAG primary antibody (1:1000; Sigma F3165) against DNA2-FLAG or anti-CtIP primary antibody (1:1000; Santa Cruz Biotechnology sc-271339) using standard procedures. To test for interactions between the pCtIP variants and MRE11 or BRCA1, 10 µL of Dynabeads protein G (Invitrogen) was conjugated with 1.5 µg of anti-CtIP antibody (1:250; Santa Cruz Biotechnology sc-271339) in PBS-T for 1 h at 4°C. Next, beads were incubated with 1 µg of the indicated recombinant pCtIP variant (bait) in IP buffer (25 mM Tris-HCl at pH 7.5, 1 mM DTT, 3 mM EDTA, 0.2 mg/mL BSA, 50 mM NaCl) for 1 h at 4°C. Beads were then washed three times with wash buffer (25 mM Tris-HCl at pH 7.5, 80 mM NaCl, 0.05% [v/v] Triton-X-100, 1 mM DTT, 3 mM EDTA) and incubated for 1 h at 4°C with 1 µg of recombinant MRE11 or BRCA1 (prey) in IP buffer. Beads were again washed three times with wash buffer, and proteins were eluted by boiling for 3 min in SDS buffer (50 mM Tris-HCl at pH 6.8, 1.6% [m/w] sodium dodecyl sulfate, 10% [v/v] glycerol, 0.1 M DTT, 0.01% [m/w] bromophenol blue). As a negative control, purified MRE11 or BRCA1 was incubated with the anti-CtIP-coupled Dynabeads that had not been bound by CtIP. The proteins in the eluate were analyzed by Western blotting using anti-CtIP primary antibody (1:1000; Santa Cruz Biotechnology sc-271339), anti-MRE11 primary antibody (1:1000; Abcam ab214), or anti-BRCA1 primary antibody (1:1000; Santa Cruz Biotechnology sc-6954) using standard procedures. To quantitate the data of the bait–prey interaction, nonspecific binding (bait without prey) signal was subtracted, and the values were normalized to the amount of bait.

In vitro kinase assays

In vitro phosphorylation reactions were performed in 20-µL volume in 50 mM Tris-HCl (pH 7.5), 5 mM magnesium acetate, 0.2 mM EDTA, 0.5 mM sodium orthovanadate (Sigma), 10 mM *p*-nitrophenyl phosphate (Sigma), 150 mM NaCl, and 1% NP-40. Recombinant pCtIP (0.7 µg) and 74 ng of PLK1 (Abcam) were added to the reactions as indicated. Reactions were initiated by the addition of 0.1 mM ATP and 37 kBq of [γ-^{32}P]ATP (Perkin Elmer) and incubated for 30 min at 37°C. Phosphorylation reactions were stopped by adding 5 µL of SDS buffer (50 mM Tris-HCl at pH 6.8, 1.6% sodium dodecyl sulfate, 10% glycerol, 0.1 M DTT, 0.01% bromophenol blue) supplemented with 1 µg of BSA and incubated for 5 min at 95°C. Samples were separated by SDS-PAGE, stained with Coomassie dye, and destained in 40% methanol and 10% acetic acid. The destained gel was dried on 3-mm paper (Whatman), exposed to storage phosphor screens (GE Healthcare), and scanned by a Typhoon 9500 phosphorimager (GE Healthcare). Phosphorylated samples used for biochemical assays were prepared as described above except for the [γ-^{32}P]ATP, which was omitted.

Competing interests statement

The authors declare no conflict of interest.

Acknowledgments

We thank members of the Cejka laboratory (A. Acharya, D. Borrello, S. Halder, V. Mengoli, G. Reginato, A. Sanchez, I. Senoussi, and M.R. Dello Stritto) for critical comments on the manuscript, and David Jarrossay for assistance with FACS analysis. This work was supported by European Research Council grants (ERC) 681630 and 101018257 and Swiss National Science Foundation grants 31003A_175444 and 310030_205199 to P.C.; Research, Development, and Innovation (R+D+I) grant PID2019-104195G from the Spanish Ministry of Science and Innovation-Agencia Estatal de Investigación 10.13039/501100011033 to P.H.; grant ANR-21-CE44-0009-01 from French government to R.G.; and Swiss National Science Foundation grant 310030_208143 to A.A.S. A.R.-F. is funded with a Formación del Profesorado Universitario (FPU) fellowship from the Spanish Ministry of Education, and R.C. is funded by a predoctoral fellowship from the Spanish Ministry of Science. Centro Andaluz de Biología Molecular y Medicina Regenerativa is supported by the regional government of Andalucia (Junta de Andalucía).

Author contributions: I.C. performed all biochemical experiments with recombinant proteins. R.T. helped performing the biochemical experiments with PLK1. E.C. prepared the *EXO1*$^{-/-}$ mammalian cell lines. I.C. performed cell biology experiments with the help of E.C. F.V. performed the coimmunoprecipitation experiment from HEK293T cells under the supervision of A.A.S. H.B. performed sequence analysis and modeling under the supervision of R.G. R.G. and H.B. performed the bioinformatics analyses and the design of the mutants. R.C. and A.R.-F. performed SMART experiments under the supervision of P.H. All authors designed the experiments and analyzed the data. I.C. and P.C. wrote the paper with input from all the authors.

References

Acharya A, Kasaciunaite K, Göse M, Kissling V, Guérois R, Seidel R, Cejka P. 2021. Distinct RPA domains promote recruitment and the helicase–nuclease activities of Dna2. *Nat Commun* **12:** 6521. doi:10.1038/s41467-021-26863-y

Anand R, Ranjha L, Cannavo E, Cejka P. 2016. Phosphorylated CtIP functions as a co-factor of the MRE11–RAD50–NBS1 endonuclease in DNA end resection. *Mol Cell* **64:** 940–950. doi:10.1016/j.molcel.2016.10.017

Anand R, Jasrotia A, Bundschuh D, Howard SM, Ranjha L, Stucki M, Cejka P. 2019. NBS1 promotes the endonuclease activity of the MRE11–RAD50 complex by sensing CtIP phosphorylation. *EMBO J* **38:** e101005. doi:10.15252/embj.2018101005

Ashkenazy H, Abadi S, Martz E, Chay O, Mayrose I, Pupko T, Ben-Tal N. 2016. Consurf 2016: an improved methodology to estimate and visualize evolutionary conservation in macromolecules. *Nucleic Acids Res* **44:** W344–W350. doi:10.1093/nar/gkw408

Bae SH, Choi E, Lee KH, Park JS, Lee SH, Seo YS. 1998. Dna2 of *Saccharomyces cerevisiae* possesses a single-stranded DNA-specific endonuclease activity that is able to act on double-stranded DNA in the presence of ATP. *J Biol Chem* **273:** 26880–26890. doi:10.1074/jbc.273.41.26880

Balbo Pogliano C, Ceppi I, Giovannini S, Petroulaki V, Palmer N, Uliana F, Gatti M, Kasaciunaite K, Freire R, Seidel R, et al. 2022. The CDK1–TOPBP1–PLK1 axis regulates the Bloom's syndrome helicase BLM to suppress crossover recombination in somatic cells. *Sci Adv* **8:** eabk0221. doi:10.1126/sciadv.abk0221

Bennardo N, Cheng A, Huang N, Stark JM. 2008. Alternative-NHEJ is a mechanistically distinct pathway of mammalian

chromosome break repair. *PLoS Genet* **4:** e1000110. doi:10.1371/journal.pgen.1000110

Bocquet N, Bizard AH, Abdulrahman W, Larsen NB, Faty M, Cavadini S, Bunker RD, Kowalczykowski SC, Cejka P, Hickson ID, et al. 2014. Structural and mechanistic insight into Holliday-junction dissolution by topoisomerase IIIα and RMI1. *Nat Struct Mol Biol* **21:** 261–268. doi:10.1038/nsmb.2775

Cannavo E, Cejka P, Kowalczykowski SC. 2013. Relationship of DNA degradation by *Saccharomyces cerevisiae* exonuclease 1 and its stimulation by RPA and Mre11–Rad50–Xrs2 to DNA end resection. *Proc Natl Acad Sci* **110:** E1661–E1668. doi:10.1073/pnas.1305166110

Cannavo E, Johnson D, Andres SN, Kissling VM, Reinert JK, Garcia V, Erie DA, Hess D, Thomä NH, Enchev RI, et al. 2018. Regulatory control of DNA end resection by Sae2 phosphorylation. *Nat Commun* **9:** 4016. doi:10.1038/s41467-018-06417-5

Cejka P, Kowalczykowski SC. 2010. The full-length *Saccharomyces cerevisiae* Sgs1 protein is a vigorous DNA helicase that preferentially unwinds Holliday junctions. *J Biol Chem* **285:** 8290–8301. doi:10.1074/jbc.M109.083196

Cejka P, Symington LS. 2021. DNA end resection: mechanism and control. *Annu Rev Genet* **55:** 285–307. doi:10.1146/annurev-genet-071719-020312

Cejka P, Cannavo E, Polaczek P, Masuda-Sasa T, Pokharel S, Campbell JL, Kowalczykowski SC. 2010. DNA end resection by Dna2–Sgs1–RPA and its stimulation by Top3–Rmi1 and Mre11–Rad50–Xrs2. *Nature* **467:** 112–116. doi:10.1038/nature09355

Ceppi I, Howard SM, Kasaciunaite K, Pinto C, Anand R, Seidel R, Cejka P. 2020. CtIP promotes the motor activity of DNA2 to accelerate long-range DNA end resection. *Proc Natl Acad Sci* **117:** 8859–8869. doi:10.1073/pnas.2001165117

Chang HHY, Pannunzio NR, Adachi N, Lieber MR. 2017. Non-homologous DNA end joining and alternative pathways to double-strand break repair. *Nat Rev Mol Cell Biol* **18:** 495–506. doi:10.1038/nrm.2017.48

Chen X, Niu H, Chung WH, Zhu Z, Papusha A, Shim EY, Lee SE, Sung P, Ira G. 2011. Cell cycle regulation of DNA double-strand break end resection by Cdk1-dependent Dna2 phosphorylation. *Nat Struct Mol Biol* **18:** 1015–1019. doi:10.1038/nsmb.2105

Chen X, Cui D, Papusha A, Zhang X, Chu CD, Tang J, Chen K, Pan X, Ira G. 2012. The Fun30 nucleosome remodeller promotes resection of DNA double-strand break ends. *Nature* **489:** 576–580. doi:10.1038/nature11355

Costelloe T, Louge R, Tomimatsu N, Mukherjee B, Martini E, Khadaroo B, Dubois K, Wiegant WW, Thierry A, Burma S, et al. 2012. The yeast Fun30 and human SMARCAD1 chromatin remodellers promote DNA end resection. *Nature* **489:** 581–584. doi:10.1038/nature11353

Daley JM, Jimenez-Sainz J, Wang W, Miller AS, Xue X, Nguyen KA, Jensen RB, Sung P. 2017. Enhancement of BLM–DNA2-mediated long-range DNA end resection by CtIP. *Cell Rep* **21:** 324–332. doi:10.1016/j.celrep.2017.09.048

Deshpande RA, Lee JH, Arora S, Paull TT. 2016. Nbs1 converts the human Mre11/Rad50 nuclease complex into an endo/exonuclease machine specific for protein-DNA adducts. *Mol Cell* **64:** 593–606. doi:10.1016/j.molcel.2016.10.010

Deshpande RA, Myler LR, Soniat MM, Makharashvili N, Lee L, Lees-Miller SP, Finkelstein IJ, Paull TT. 2020. DNA-dependent protein kinase promotes DNA end processing by MRN and CtIP. *Sci Adv* **6:** eaay0922. doi:10.1126/sciadv.aay0922

Dong S, Han J, Chen H, Liu T, Huen MSY, Yang Y, Guo C, Huang J. 2014. The human SRCAP chromatin remodeling complex promotes DNA-end resection. *Curr Biol* **24:** 2097–2110. doi:10.1016/j.cub.2014.07.081

Eid W, Steger M, El-Shemerly M, Ferretti LP, Pena-Diaz J, König C, Valtorta E, Sartori AA, Ferrari S. 2010. DNA end resection by CtIP and exonuclease 1 prevents genomic instability. *EMBO Rep* **11:** 962–968. doi:10.1038/embor.2010.157

Emam A, Wu X, Xu S, Wang L, Liu S, Wang B. 2022. Stalled replication fork protection limits cGAS-STING and P-body-dependent innate immune signalling. *Nat Cell Biol* **24:** 1154–1164. doi:10.1038/s41556-022-00950-8

Evans R, O'Neill M, Pritzel A, Antropova N, Senior A, Green T, Žídek A, Bates R, Blackwell S, Yim J, et al. 2022. Protein complex prediction with AlphaFold–Multimer. *bioRxiv* doi:10.1101/2021.10.04.463034

Ferretti LP, Lafranchi L, Sartori AA. 2013. Controlling DNA-end resection: a new task for CDKs. *Front Genet* **4:** 99. doi:10.3389/fgene.2013.00099

Ferretti LP, Himmels SF, Trenner A, Walker C, von Aesch C, Eggenschwiler A, Murina O, Enchev RI, Peter M, Freire R, et al. 2016. Cullin3-KLHL15 ubiquitin ligase mediates CtIP protein turnover to fine-tune DNA-end resection. *Nat Commun* **7:** 12628. doi:10.1038/ncomms12628

Forment JV, Walker RV, Jackson SP. 2012. A high-throughput, flow cytometry-based method to quantify DNA-end resection in mammalian cells. *Cytometry A* **81A:** 922–928. doi:10.1002/cyto.a.22155

Gobbini E, Cassani C, Vertemara J, Wang W, Mambretti F, Casari E, Sung P, Tisi R, Zampella G, Longhese MP. 2018. The MRX complex regulates Exo1 resection activity by altering DNA end structure. *EMBO J* **37:** e98588. doi:10.15252/embj.201798588

Gravel S, Chapman JR, Magill C, Jackson SP. 2008. DNA helicases Sgs1 and BLM promote DNA double-strand break resection. *Genes Dev* **22:** 2767–2772. doi:10.1101/gad.503108

Han J, Wan L, Jiang G, Cao L, Xia F, Tian T, Zhu X, Wu M, Huen MSY, Wang Y, et al. 2021. ATM controls the extent of DNA end resection by eliciting sequential posttranslational modifications of CtIP. *Proc Natl Acad Sci* **118:** e2022600118. doi:10.1073/pnas.2022600118

Huertas P, Cruz-García A. 2018. Single molecule analysis of resection tracks. *Methods Mol Biol* **1672:** 147–154. doi:10.1007/978-1-4939-7306-4_12

Huertas P, Jackson SP. 2009. Human CtIP mediates cell cycle control of DNA end resection and double strand break repair. *J Biol Chem* **284:** 9558–9565. doi:10.1074/jbc.M808906200

Huertas P, Cortés-Ledesma F, Sartori AA, Aguilera A, Jackson SP. 2008. CDK targets Sae2 to control DNA-end resection and homologous recombination. *Nature* **455:** 689–692. doi:10.1038/nature07215

Ira G, Pellicioli A, Balijja A, Wang X, Fiorani S, Carotenuto W, Liberi G, Bressan D, Wan L, Hollingsworth NM, et al. 2004. DNA end resection, homologous recombination and DNA damage checkpoint activation require CDK1. *Nature* **431:** 1011–1017. doi:10.1038/nature02964

Isobe SY, Hiraga SI, Nagao K, Sasanuma H, Donaldson AD, Obuse C. 2021. Protein phosphatase 1 acts as a RIF1 effector to suppress DSB resection prior to Shieldin action. *Cell Rep* **36:** 109383. doi:10.1016/j.celrep.2021.109383

Jumper J, Evans R, Pritzel A, Green T, Figurnov M, Ronneberger O, Tunyasuvunakool K, Bates R, Žídek A, Potapenko A, et al. 2021. Highly accurate protein structure prediction with AlphaFold. *Nature* **596:** 583–589. doi:10.1038/s41586-021-03819-2

Katoh K, Standley DM. 2013. MAFFT multiple sequence alignment software version 7: improvements in performance and

usability. *Mol Biol Evol* **30:** 772–780. doi:10.1093/molbev/mst010

Kollárovič G, Topping CE, Shaw EP, Chambers AL. 2020. The human HELLS chromatin remodelling protein promotes end resection to facilitate homologous recombination and contributes to DSB repair within heterochromatin. *Nucleic Acids Res* **48:** 1872–1885. doi:10.1093/nar/gkz1146

Leman JK, Weitzner BD, Lewis SM, Adolf-Bryfogle J, Alam N, Alford RF, Aprahamian M, Baker D, Barlow KA, Barth P, et al. 2020. Macromolecular modeling and design in Rosetta: recent methods and frameworks. *Nat Methods* **17:** 665–680. doi:10.1038/s41592-020-0848-2

Levikova M, Pinto C, Cejka P. 2017. The motor activity of DNA2 functions as an ssDNA translocase to promote DNA end resection. *Genes Dev* **31:** 493–502. doi:10.1101/gad.295196.116

Li F, Mladenov E, Mortoga S, Iliakis G. 2020. SCF^{SKP2} regulates APC/C^{CDH1}-mediated degradation of CTIP to adjust DNA-end resection in G_2-phase. *Cell Death Dis* **11:** 548. doi:10.1038/s41419-020-02755-9

Mariotti L, Wild S, Brunoldi G, Piceni A, Ceppi I, Kummer S, Lutz RE, Cejka P, Gari K. 2020. The iron–sulphur cluster in human DNA2 is required for all biochemical activities of DNA2. *Commun Biol* **3:** 322. doi:10.1038/s42003-020-1048-4

Masuda-Sasa T, Imamura O, Campbell JL. 2006. Biochemical analysis of human Dna2. *Nucleic Acids Res* **34:** 1865–1875. doi:10.1093/nar/gkl070

Miller AS, Daley JM, Pham NT, Niu H, Xue X, Ira G, Sung P. 2017. A novel role of the Dna2 translocase function in DNA break resection. *Genes Dev* **31:** 503–510. doi:10.1101/gad.295659.116

Mimitou EP, Symington LS. 2008. Sae2, Exo1 and Sgs1 collaborate in DNA double-strand break processing. *Nature* **455:** 770–774. doi:10.1038/nature07312

Mirdita M, von den Driesch L, Galiez C, Martin MJ, Söding J, Steinegger M. 2017. Uniclust databases of clustered and deeply annotated protein sequences and alignments. *Nucleic Acids Res* **45:** D170–D176. doi:10.1093/nar/gkw1081

Mirdita M, Schütze K, Moriwaki Y, Heo L, Ovchinnikov S, Steinegger M. 2022. Colabfold: making protein folding accessible to all. *Nat Methods* **19:** 679–682. doi:10.1038/s41592-022-01488-1

Nakamura K, Kogame T, Oshiumi H, Shinohara A, Sumitomo Y, Agama K, Pommier Y, Tsutsui KM, Tsutsui K, Hartsuiker E, et al. 2010. Collaborative action of Brca1 and CtIP in elimination of covalent modifications from double-strand breaks to facilitate subsequent break repair. *PLoS Genet* **6:** e1000828. doi:10.1371/journal.pgen.1000828

Nimonkar AV, Genschel J, Kinoshita E, Polaczek P, Campbell JL, Wyman C, Modrich P, Kowalczykowski SC. 2011. BLM–DNA2–RPA–MRN and EXO1–BLM–RPA–MRN constitute two DNA end resection machineries for human DNA break repair. *Genes Dev* **25:** 350–362. doi:10.1101/gad.2003811

Peterson SE, Li Y, Wu-Baer F, Chait BT, Baer R, Yan H, Gottesman ME, Gautier J. 2013. Activation of DSB processing requires phosphorylation of CtIP by ATR. *Mol Cell* **49:** 657–667. doi:10.1016/j.molcel.2012.11.020

Pinto C, Kasaciunaite K, Seidel R, Cejka P. 2016. Human DNA2 possesses a cryptic DNA unwinding activity that functionally integrates with BLM or WRN helicases. *Elife* **5:** e18574. doi:10.7554/eLife.18574

Przetocka S, Porro A, Bolck HA, Walker C, Lezaja A, Trenner A, von Aesch C, Himmels SF, D'Andrea AD, Ceccaldi R, et al. 2018. CtIP-mediated fork protection synergizes with BRCA1 to suppress genomic instability upon DNA replication stress. *Mol Cell* **72:** 568–582.e6. doi:10.1016/j.molcel.2018.09.014

Pupko T, Bell RE, Mayrose I, Glaser F, Ben-Tal N. 2002. Rate4Site: an algorithmic tool for the identification of functional regions in proteins by surface mapping of evolutionary determinants within their homologues. *Bioinformatics* **18 Suppl 1:** S71–S77. doi:10.1093/bioinformatics/18.suppl_1.S71

Ranjha L, Howard SM, Cejka P. 2018. Main steps in DNA double-strand break repair: an introduction to homologous recombination and related processes. *Chromosoma* **127:** 187–214. doi:10.1007/s00412-017-0658-1

Reginato G, Cannavo E, Cejka P. 2017. Physiological protein blocks direct the Mre11–Rad50–Xrs2 and Sae2 nuclease complex to initiate DNA end resection. *Genes Dev* **31:** 2325–2330. doi:10.1101/gad.308254.117

Sartori AA, Lukas C, Coates J, Mistrik M, Fu S, Bartek J, Baer R, Lukas J, Jackson SP. 2007. Human CtIP promotes DNA end resection. *Nature* **450:** 509–514. doi:10.1038/nature06337

Shen J, Zhao Y, Pham NT, Li Y, Zhang Y, Trinidad J, Ira G, Qi Z, Niu H. 2022. Deciphering the mechanism of processive ssDNA digestion by the Dna2–RPA ensemble. *Nat Commun* **13:** 359. doi:10.1038/s41467-021-27940-y

Shibata A, Moiani D, Arvai AS, Perry J, Harding SM, Genois MM, Maity R, van Rossum-Fikkert S, Kertokalio A, Romoli F, et al. 2014. DNA double-strand break repair pathway choice is directed by distinct MRE11 nuclease activities. *Mol Cell* **53:** 7–18. doi:10.1016/j.molcel.2013.11.003

Shim EY, Chung WH, Nicolette ML, Zhang Y, Davis M, Zhu Z, Paull TT, Ira G, Lee SE. 2010. Saccharomyces cerevisiae Mre11/Rad50/Xrs2 and Ku proteins regulate association of Exo1 and Dna2 with DNA breaks. *EMBO J* **29:** 3370–3380. doi:10.1038/emboj.2010.219

Soniat MM, Myler LR, Kuo HC, Paull TT, Finkelstein IJ. 2019. RPA phosphorylation inhibits DNA resection. *Mol Cell* **75:** 145–153.e5. doi:10.1016/j.molcel.2019.05.005

Stark JM, Pierce AJ, Oh J, Pastink A, Jasin M. 2004. Genetic steps of mammalian homologous repair with distinct mutagenic consequences. *Mol Cell Biol* **24:** 9305–9316. doi:10.1128/MCB.24.21.9305-9316.2004

Steinegger M, Meier M, Mirdita M, Vöhringer H, Haunsberger SJ, Söding J. 2019. HH-suite3 for fast remote homology detection and deep protein annotation. *BMC Bioinformatics* **20:** 473. doi:10.1186/s12859-019-3019-7

Sturzenegger A, Burdova K, Kanagaraj R, Levikova M, Pinto C, Cejka P, Janscak P. 2014. DNA2 cooperates with the WRN and BLM RecQ helicases to mediate long-range DNA end resection in human cells. *J Biol Chem* **289:** 27314–27326. doi:10.1074/jbc.M114.578823

Tran PT, Erdeniz N, Dudley S, Liskay RM. 2002. Characterization of nuclease-dependent functions of Exo1p in *Saccharomyces cerevisiae*. *DNA Repair* **1:** 895–912. doi:10.1016/S1568-7864(02)00114-3

Wang H, Shi LZ, Wong CC, Han X, Hwang PY, Truong LN, Zhu Q, Shao Z, Chen DJ, Berns MW, et al. 2013. The interaction of CtIP and Nbs1 connects CDK and ATM to regulate HR-mediated double-strand break repair. *PLoS Genet* **9:** e1003277. doi:10.1371/journal.pgen.1003277

Wang H, Qiu Z, Liu B, Wu Y, Ren J, Liu Y, Zhao Y, Wang Y, Hao S, Li Z, et al. 2018. PLK1 targets CtIP to promote microhomology-mediated end joining. *Nucleic Acids Res* **46:** 10724–10739.

Waterhouse AM, Procter JB, Martin DM, Clamp M, Barton GJ. 2009. Jalview version 2—a multiple sequence alignment editor and analysis workbench. *Bioinformatics* **25:** 1189–1191. doi:10.1093/bioinformatics/btp033

West SC, Blanco MG, Chan YW, Matos J, Sarbajna S, Wyatt HD. 2015. Resolution of recombination intermediates: mechanisms and regulation. *Cold Spring Harb Symp Quant Biol* **80:** 103–109. doi:10.1101/sqb.2015.80.027649

Zhou Y, Caron P, Legube G, Paull TT. 2014. Quantitation of DNA double-strand break resection intermediates in human cells. *Nucleic Acids Res* **42:** e19. doi:10.1093/nar/gkt1309

Zhou C, Pourmal S, Pavletich NP. 2015. Dna2 nuclease-helicase structure, mechanism and regulation by Rpa. *Elife* **4:** e09832. doi:10.7554/eLife.09832

Zhu Z, Chung WH, Shim EY, Lee SE, Ira G. 2008. Sgs1 helicase and two nucleases Dna2 and Exo1 resect DNA double-strand break ends. *Cell* **134:** 981–994. doi:10.1016/j.cell.2008.08.037

PLK1 regulates CtIP and DNA2 interplay in long-range DNA end resection

Ilaria Ceppi, Elda Cannavo, Hélène Bret, et al.

Genes Dev. 2023, **37:** originally published online February 6, 2023
Access the most recent version at doi:10.1101/gad.349981.122